





## Article

# Oxygen Nonstoichiometry, Electrical Conductivity, Chemical Expansion and Electrode Properties of Perovskite-Type $\text{SrFe}_{0.9}\text{V}_{0.1}\text{O}_{3-\delta}$

Aleksei I. Ivanov <sup>1,\*</sup>, Sergey S. Nikitin <sup>1</sup>, Mariya S. Dyakina <sup>1</sup>, Ekaterina V. Tsipis <sup>1,\*</sup>, Mikhail V. Patrakeev <sup>1</sup>, Dmitrii A. Agarkov <sup>1,2</sup>, Irina I. Zverkova <sup>1</sup>, Andrey O. Zhigachev <sup>1</sup>, Victor V. Kedrov <sup>1</sup> and Vladislav V. Kharton <sup>1</sup>

<sup>1</sup> Osipyan Institute of Solid State Physics RAS, Chernogolovka 142432, Russia; nikitin@issp.ac.ru (S.S.N.); dyakina@issp.ac.ru (M.S.D.); patrakeev@issp.ac.ru (M.V.P.); agarkov@issp.ac.ru (D.A.A.); zverkova@issp.ac.ru (I.I.Z.); zhigachev@issp.ac.ru (A.O.Z.); kedr@issp.ac.ru (V.V.K.); kharton@issp.ac.ru (V.V.K.)

<sup>2</sup> Moscow Institute of Physics and Technology, Dolgoprudny 141701, Russia

\* Correspondence: aliv@issp.ac.ru (A.I.I.); tsipis@issp.ac.ru (E.V.T.)

**Abstract:** X-ray diffraction analysis of the pseudo-binary  $\text{SrFe}_{1-x}\text{V}_x\text{O}_{3-\delta}$  system showed that the solid solution formation limit at atmospheric oxygen pressure corresponds to  $x \approx 0.1$ .  $\text{SrFe}_{0.9}\text{V}_{0.1}\text{O}_{3-\delta}$  has a cubic perovskite-type structure with the  $Pm\bar{3}m$  space group. The oxygen nonstoichiometry variations in  $\text{SrFe}_{0.9}\text{V}_{0.1}\text{O}_{3-\delta}$ , measured by coulometric titration in the oxygen partial pressure range of  $10^{-21}$  to 0.5 atm at 1023–1223 K, can be adequately described using an ideal solution approximation with  $\text{V}^{5+}$  as the main oxidation state of vanadium cations. This approach was additionally validated by statistical thermodynamic modeling. The incorporation of vanadium decreases both oxygen deficiency and the average iron oxidation state with respect to undoped  $\text{SrFeO}_{3-\delta}$ . As a result, the electrical conductivity, thermal expansion and chemical expansivity associated with the oxygen vacancy formation all become lower compared to strontium ferrite. At 923 K, the conductivity of  $\text{SrFe}_{0.9}\text{V}_{0.1}\text{O}_{3-\delta}$  is 14% lower than that of  $\text{SrFeO}_{3-\delta}$  but 21% higher compared to  $\text{SrFe}_{0.9}\text{Ta}_{0.1}\text{O}_{3-\delta}$ . The area-specific polarization resistance of the porous  $\text{SrFe}_{0.9}\text{V}_{0.1}\text{O}_{3-\delta}$  electrode deposited onto 10 mol.% scandia- and 1 mol.% yttria-co-stabilized zirconia solid electrolyte with a protective  $\text{Ce}_{0.9}\text{Gd}_{0.1}\text{O}_{2-\delta}$  interlayer, was 0.34  $\text{Ohm} \times \text{cm}^2$  under open-circuit conditions at 1173 K in air.

**Keywords:** vanadium-doped strontium ferrite; defect structure; electrical conductivity; thermal expansion; chemical expansion; SOFC/SOEC electrodes



Academic Editor: Federico Bella

Received: 19 September 2024

Revised: 16 December 2024

Accepted: 17 January 2025

Published: 22 January 2025

**Citation:** Ivanov, A.I.; Nikitin, S.S.; Dyakina, M.S.; Tsipis, E.V.; Patrakeev, M.V.; Agarkov, D.A.; Zverkova, I.I.; Zhigachev, A.O.; Kedrov, V.V.; Kharton, V.V. Oxygen

Nonstoichiometry, Electrical Conductivity, Chemical Expansion and Electrode Properties of Perovskite-Type  $\text{SrFe}_{0.9}\text{V}_{0.1}\text{O}_{3-\delta}$ . *Materials* **2025**, *18*, 493. <https://doi.org/10.3390/ma18030493>

**Copyright:** © 2025 by the authors. Licensee MDPI, Basel, Switzerland. This article is an open access article distributed under the terms and conditions of the Creative Commons Attribution (CC BY) license (<https://creativecommons.org/licenses/by/4.0/>).

## 1. Introduction

In recent years, structural features and transport properties of perovskite-type strontium ferrite ( $\text{SrFeO}_{3-\delta}$ ) have attracted significant attention due to its wide range of oxygen deficiency ( $2.5 \leq (3 - \delta) \leq 3$ ) and high mixed ionic–electronic conductivity [1–7]. However, the practical applications of  $\text{SrFeO}_{3-\delta}$  in high- and intermediate-temperature electrochemical devices are limited by several factors. First, an increase in oxygen nonstoichiometry under reducing conditions leads to phase transition into orthorhombic brownmillerite, which is accompanied by a substantial decrease in conductivity and large volume changes [1,3,4]. Second, the oxygen release from an  $\text{SrFeO}_{3-\delta}$  crystal lattice on heating results in a drastic increase in the apparent average thermal expansion coefficient (TEC) due to the so-called chemical contribution [2,3,7,8]. Third, at atmospheric oxygen pressure, the cubic structure

of  $\text{SrFeO}_{3-\delta}$  perovskite only exists at elevated temperatures; its tetragonal polymorph is formed on cooling down to room temperature, again with volume changes [2,3,8]. Notice that the cubic vacancy-disordered structure of  $\text{SrFeO}_{3-\delta}$  with the space group (SG)  $Pm\bar{3}m$  provides the highest level of mixed conductivity due to the isotropic transport of electronic and ionic charge carriers [4,8].

Another material to attract attention is perovskite-type strontium vanadate ( $\text{SrVO}_{3-\delta}$ ). This phase exhibits moderate apparent TEC and high electronic conductivity under reducing conditions, namely  $\sim 10^3$  S/cm at the oxygen partial pressure ( $p(\text{O}_2)$ ) of  $10^{-20}$  atm [9–12].  $\text{SrVO}_{3-\delta}$  and its La-substituted analogues are widely considered as anode materials for solid oxide fuel cells (SOFCs) using both hydrogen and cheaper hydrocarbon-based fuels; in particular, those containing  $\text{H}_2\text{S}$  and other harmful impurities [13,14]. The main disadvantage of  $\text{SrVO}_{3-\delta}$  relates to phase instability on redox cycling [10,12,15]. When  $\text{SrVO}_{3-\delta}$  is annealed in air, phase decomposition leads to a decrease in electrical conductivity by approximately six orders of magnitude and to significant volume expansion [10,12,15]. Moreover, this decomposition may be irreversible [10].

Taking into account the advantages of  $\text{SrFeO}_3$ - and  $\text{SrVO}_3$ -based materials, the present work was centered on studies of the pseudo-binary  $\text{SrFe}_{1-x}\text{V}_x\text{O}_{3-\delta}$  system. Particular attention was paid to the functional properties important for the electrodes of SOFCs and solid oxide electrolysis cells (SOECs). Doping of  $\text{SrFeO}_{3-\delta}$  with higher-valency cations (e.g., Nb, Ta, Mo or W) having predominant octahedral coordination with oxygen is well known to stabilize the cubic perovskite structure in a wide temperature range, to suppress the “perovskite  $\rightarrow$  brownmillerite” transition under reducing conditions, and to decrease apparent TECs [5–7,16–20]. High-resolution electron microscopic analysis of  $\text{SrFe}_{1-x}\text{V}_x\text{O}_{3-\delta}$ , synthesized in an evacuated quartz tube with quenching from 1473 K, showed that vanadium doping does indeed have a noticeable effect on the structure, even at low dopant concentrations [21]. Namely, although the formation of nanodomains ( $\leq 20$  nm) with a brownmillerite structure was observed in the compositional range of  $0.05 \leq x \leq 0.10$ , the presence of vanadium and excess oxygen blocked nanodomain growth [21]. Similar conclusions have been drawn for  $\text{SrFe}_{1-x}\text{V}_x\text{O}_{3-\delta}$  ( $0 \leq x \leq 0.08$ ) synthesized in a vacuum followed by quenching from 1173–1223 K [22,23]. The formation of  $\text{ALaFeVO}_6$  ( $A = \text{Ca}, \text{Sr}$ ) double perovskites was achieved by annealing in evacuated and sealed silica tubes at 1273 K for 8 days [24]. Such synthetic approaches cannot, however, be effective for SOFC/SOEC technologies, as each porous electrode in these devices is unavoidably equilibrated with the relevant atmosphere at elevated temperatures. In the present work, synthesis of  $\text{SrFe}_{1-x}\text{V}_x\text{O}_{3-\delta}$  was performed in atmospheric air.

## 2. Materials and Methods

The synthesis of  $\text{SrFe}_{1-x}\text{V}_x\text{O}_{3-\delta}$  ( $x = 0.10, 0.15$  and  $0.20$ ) powders was carried out by the citrate–nitrate method using  $\text{Sr}(\text{NO}_3)_2$ ,  $\text{FeC}_2\text{O}_4 \cdot 2\text{H}_2\text{O}$ ,  $\text{NH}_4\text{VO}_3$  and  $\text{C}_6\text{H}_8\text{O}_7 \cdot \text{H}_2\text{O}$  ( $\geq 99\%$  purity) as starting reagents. Notice that combustion synthesis routes are often used for commercial-scale applications. At the initial stage of the synthesis,  $\text{Sr}(\text{NO}_3)_2$ ,  $\text{NH}_4\text{VO}_3$  and  $\text{C}_6\text{H}_8\text{O}_7 \cdot \text{H}_2\text{O}$  were dissolved in distilled water with vigorous stirring; citric acid was taken in threefold excess with respect to the metal cations introduced in the stoichiometric ratio. The stoichiometric amount of iron oxalate was separately dissolved in dilute nitric acid. Then, the solutions were mixed and evaporated. Further smoldering of the mixtures resulted in fine powders, which were calcined in air at 1173 K for 2 h to remove the organic residues. Following careful grinding, the final annealing step was carried out in air during 10 h at 1373–1473 K with a heating/cooling rate of 3 K/min. The synthesized powders were ball-milled in ethanol media at 400 rpm for 2 h using a Fritsch planetary ball mill with containers and balls made of partially stabilized zirconia. Ceramic samples were obtained by uniaxial

pressing in the form of disks (diameter of 20 mm and thickness of 2–3 mm) at ~200 MPa and sintered in air at 1553 K for 2 h. For the studies of transport and thermomechanical properties, rectangular bars ( $2 \times 2 \times 10 \text{ mm}^3$ ) were cut from the sintered disks. The microstructure of the powders, ceramics and model electrochemical cells was analyzed using scanning electron microscopy (SEM, LEO SUPRA 50VP, Carl Zeiss, Oberkochen, Germany) combined with energy-dispersive X-ray spectroscopy (EDX) analyses.

X-ray diffraction (XRD) analysis was performed at room temperature on a Rigaku SmartLab SE diffractometer ( $\text{CuK}\alpha$  radiation,  $20^\circ \leq 2\theta \leq 80^\circ$ ). Phase analysis of the samples and calculation of lattice parameters were performed using Match and PowderCell (version 2.4) software. The particle size distributions of the powders were assessed by static laser light scattering (Analysette 22 Next Nano, Fritsch, Luxemburg, Luxemburg). Prior to the analysis, the powders were dispersed in bi-distilled water employing ultrasonic radiation. In order to evaluate stability under reducing conditions, powdered  $\text{SrFe}_{1-x}\text{V}_x\text{O}_{3-\delta}$  samples were annealed in a 4%  $\text{H}_2$ -Ar- $\text{H}_2\text{O}$  gas mixture where the oxygen partial pressure was controlled using a zirconia electrochemical sensor. Thermogravimetric analysis (TGA) was carried out in flowing atmospheric air using a Setaram Setsys EVO 16 instrument (Setaram, Caluire, France); the measurements were performed in a cooling mode (1 K/min) after equilibration at 1223 K for 5 h. The electrical conductivity was measured by the 4-probe DC technique at 473–1223 K in air and Ar flows.

The variations of oxygen nonstoichiometry were studied by coulometric titration in a  $p(\text{O}_2)$  range of  $10^{-21}$ –0.5 atm at 1023–1223 K with a step of 50 K in the  $\text{CO}_2$ -CO- $\text{O}_2$  gas system. The measurements were performed using a double electrochemical cell, equipped with an oxygen pump and a sensor, made of stabilized zirconia with porous Pt electrodes. The experimental data points were recorded after equilibration of the sample with the gas phase. The equilibrium criteria included the rate of changes in the logarithm of  $p(\text{O}_2)$  less than  $10^{-4}$  per minute and the standard deviation from a mean value lower than 0.03% at fixed temperature. The reliability of the collected data was evaluated using reproducibility analysis in the course of thermo or redox cycling. The measurement procedures and equipment were detailed elsewhere [5].

Thermal expansion of the ceramic materials in air and argon was tested using a Linseis L75VS1400 vertical alumina dilatometer (Linseis, Selb, Germany). The measurements were conducted in dynamic and static regimes. In dynamic mode, the sample was continuously heated at a rate of 3 K/min up to 1273 K, equilibrated for 2 h at this temperature and then cooled down to 373 K at the same rate. In static mode, the sample was heated up to 1273 K, followed by stepwise cooling down to 873 K (step 50 K) with isothermal equilibration dwells at each temperature. Examples illustrating this measuring mode for  $\text{SrFe}_{0.9}\text{V}_{0.1}\text{O}_{3-\delta}$  are presented in Electronic Supplementary Materials (Figure S1). The isothermal chemical expansion ( $\epsilon_{\text{chem}}$ ) on “air  $\rightarrow$  argon” transition at temperature  $T$  was calculated by the equation

$$\epsilon_{\text{chem}} = \frac{L_{\text{Ar},T} - L_{\text{air},T}}{L_{\text{air},T}} \quad (1)$$

where  $L_{\text{Ar},T}$  and  $L_{\text{air},T}$  are the sample length values in argon and air, respectively.

The electrochemical tests of porous electrode layers were carried out by the 3-electrode technique, as reported elsewhere [25,26]. The model half-cells comprised one gas-tight disk (1 mm thick) of 10 mol.% scandia- and 1 mol.% yttria-co-stabilized zirconia solid electrolyte (10Sc1YSZ, DKKK, Osaka, Japan), a working electrode (WE) of porous  $\text{SrFe}_{1-x}\text{V}_x\text{O}_{3-\delta}$  deposited onto a protective  $\text{Ce}_{0.9}\text{Gd}_{0.1}\text{O}_{2-\delta}$  (GDC10, Kceracell, Geumsan-gun, Republic of Korea) interlayer, and porous Pt counter and reference electrodes (CE and RE, respectively). The oxide layers were made of inks containing ball-milled powders, V-006A binder (Heraeus GmbH, Hanau, Germany) and terpeneol. The protective GDC10 interlayer (semi-

circular with a geometric area of 1.2 cm<sup>2</sup>) was first screen-printed onto one side of the electrolyte membrane, followed by sintering at 1473 K for 2 h. Then GDC10 was screen-printed again and, after drying at 373 K, the WE layer was deposited. The protective interlayer and WE were sintered in air at 1373 K for 2 h with a heating/cooling rate of 4 K/min. The CE, symmetrically with respect to the WE, was applied onto the opposite side of the solid electrolyte. The RE (~1 mm in diameter) was placed at a distance of at least 6 mm from the WE. The platinum CE and RE were annealed in air at 1223 K for 30 min. A Pt mesh and Pt wire were used as current collectors for the WE and CE, respectively. Neither additional layers nor other noble metals were applied on the WE surface in order to avoid possible contributions to its electrochemical performance. The measurements were performed using an AutoLab PGSTAT302N potentiostat/galvanostat (Metrohm, Utrecht, The Netherlands) at 1023–1173 K in static air. The relaxation time after a change in the WE potential was 60 min. Ohmic and polarization resistance values were extracted from impedance spectra collected in a frequency range from 1 MHz down to 0.1 Hz.

### 3. Results and Discussion

#### 3.1. Phase Relationships and Crystal Structure

XRD patterns of SrFe<sub>1-x</sub>V<sub>x</sub>O<sub>3-δ</sub> ( $x = 0.10\text{--}0.20$ ) synthesized in air are presented in Figure 1. The composition with  $x = 0.1$  is single phase and has a cubic perovskite-type structure (SG  $Pm\bar{3}m$ ) and a unit cell parameter  $a = 3.8947 \pm 0.0003$  Å. Note that, for undoped SrFeO<sub>3-δ</sub> prepared in the same conditions [5], a tetragonal polymorph with SG  $I4/mmm$  is formed. Reduction of SrFe<sub>0.9</sub>V<sub>0.1</sub>O<sub>3-δ</sub> in a flow of 4% H<sub>2</sub>-Ar-H<sub>2</sub>O gas mixture at 1123 K and  $p(\text{O}_2) \approx 10^{-18}$  atm results in the segregation of Sr<sub>4</sub>Fe<sub>6</sub>O<sub>13</sub> and Sr<sub>6</sub>V<sub>2</sub>O<sub>11</sub> impurities. This behavior indicates that, although the incorporation of 10% vanadium in the iron sublattice of strontium ferrite stabilizes the cubic perovskite phase down to room temperature in air, the thermodynamic stability of SrFe<sub>0.9</sub>V<sub>0.1</sub>O<sub>3-δ</sub> under reducing conditions is insufficient for use as an SOFC anode or SOEC cathode material, even in mild reducing atmospheres. At the same time, the latter composition is close to the solid solution formation limit in an SrFe<sub>1-x</sub>V<sub>x</sub>O<sub>3-δ</sub> system. In the case of  $x = 0.15\text{--}0.20$ , the peaks of Sr<sub>3</sub>(VO<sub>4</sub>)<sub>2</sub> impurity are visible in the XRD patterns, either after synthesis in air or after reduction at 1223 K and  $p(\text{O}_2) \approx 10^{-16}$  atm. Consequently, SrFe<sub>0.85</sub>V<sub>0.15</sub>O<sub>3-δ</sub> and SrFe<sub>0.8</sub>V<sub>0.2</sub>O<sub>3-δ</sub> were excluded from further studies.

#### 3.2. Microstructure

A typical SEM micrograph illustrating the powder morphology after final annealing in air at 1473 K is shown in Figure 2a. The powder consists of submicron and micron-size particles and is highly agglomerated. Static laser scattering (Figure 3) shows that the majority of the agglomerates are fairly large, with an average of 9 μm. There are also significant amounts of small agglomerates or individual particles of approximately 2 μm in size and a small number of large 40 μm agglomerates. The electrode layers made of this powder possess a low porosity and poor adhesion to the protective GDC10 interlayer (Figure 2c). Therefore, in order to prepare inks for screen printing the electrode layers used for the electrochemical measurements, the powders were milled. The resultant powder consists of fine submicron particles (Figure 2b) forming small agglomerates with average sizes of about 1 μm and 10 μm with an approximate ratio of 4:1 (Figure 3).

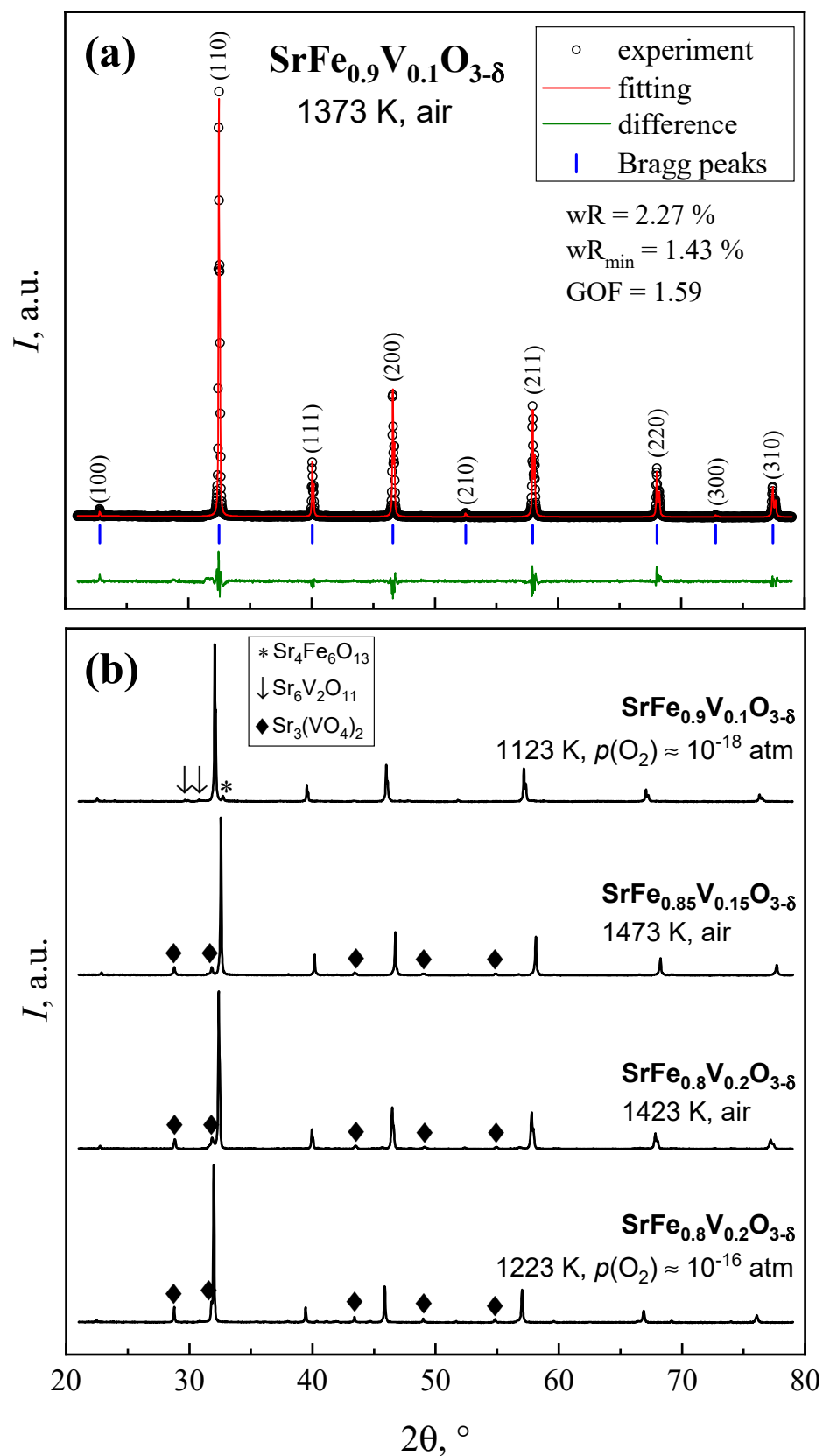


**Figure 1.** Room temperature XRD pattern of  $\text{SrFe}_{0.9}\text{V}_{0.1}\text{O}_{3-\delta}$  powder after synthesis in air (a) and of  $\text{SrFe}_{1-x}\text{V}_x\text{O}_{3-\delta}$  powders after synthesis in air and annealing in reducing conditions (b).

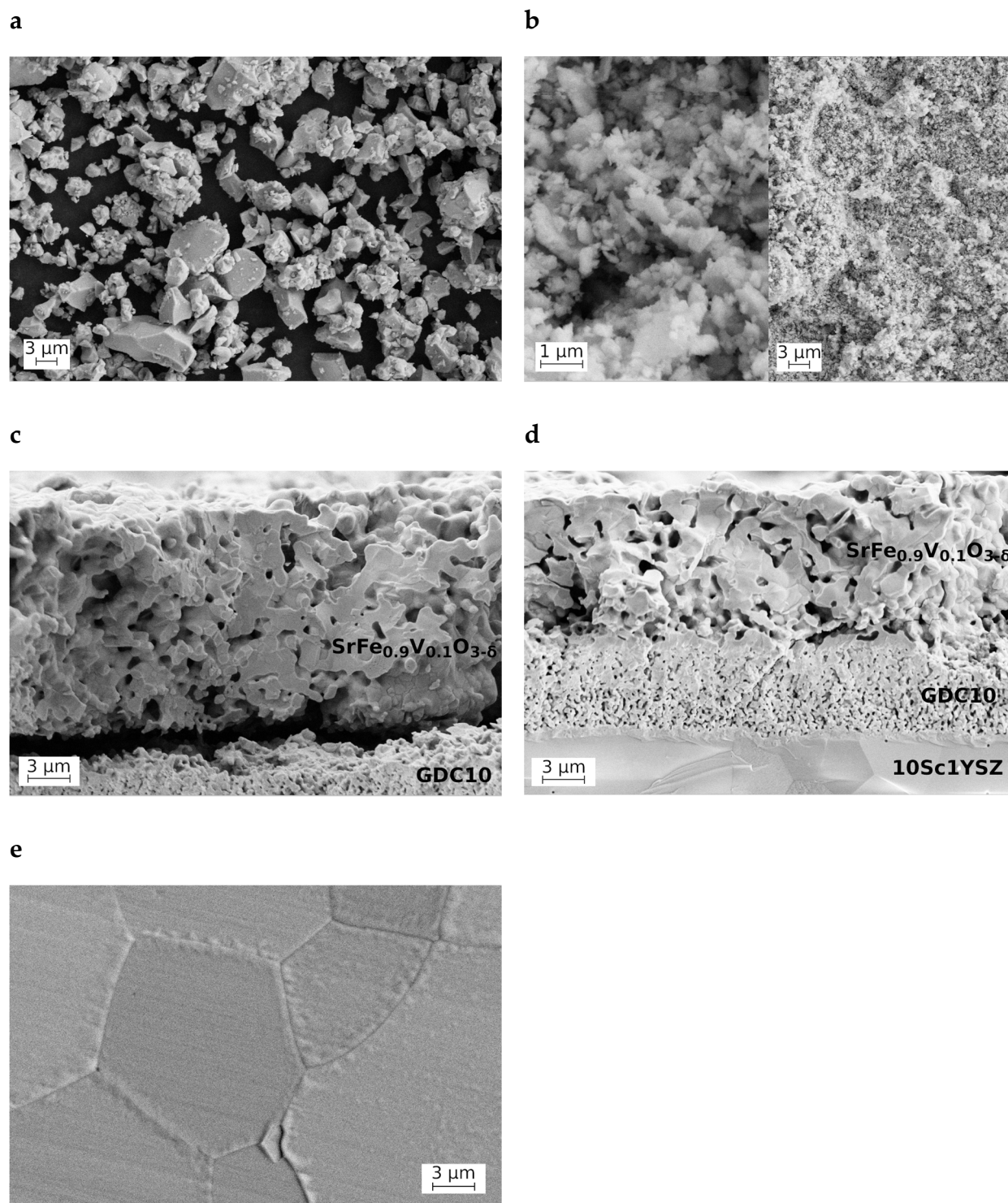


**Figure 2.** SEM micrographs of  $\text{SrFe}_{0.9}\text{V}_{0.1}\text{O}_{3-\delta}$  powder as-synthesized (a) and after ball-milling (b), and porous electrode layers (cross-sections of the electrochemical cells) made of as-synthesized (c) and milled (d) powders sintered in air at 1473 K, and dense ceramics sintered at 1553 K (e).

Figure 2d displays cross-sections of the electrochemical cell comprising 10Sc1YSZ solid electrolyte, protective GDC10 interlayer, and  $\text{SrFe}_{0.9}\text{V}_{0.1}\text{O}_{3-\delta}$  working electrode. The ceria-based interlayer with a thickness of  $\sim 6 \mu\text{m}$  shows good adhesion to the dense electrolyte membrane and to the WE. The porous  $\text{SrFe}_{0.9}\text{V}_{0.1}\text{O}_{3-\delta}$  electrode is built of micron-scale particles ( $0.5\text{--}2 \mu\text{m}$  in size) and has a thickness of  $\sim 11 \mu\text{m}$ . The cell with this microstructure was selected for further studies.

Figure 2e illustrates the microstructure of  $\text{SrFe}_{0.9}\text{V}_{0.1}\text{O}_{3-\delta}$  ceramics used for thermo-mechanical and electrical measurements. The grain size varied in the range of 4–10  $\mu\text{m}$ . No visible inhomogeneities were detected by SEM/EDX analyses.

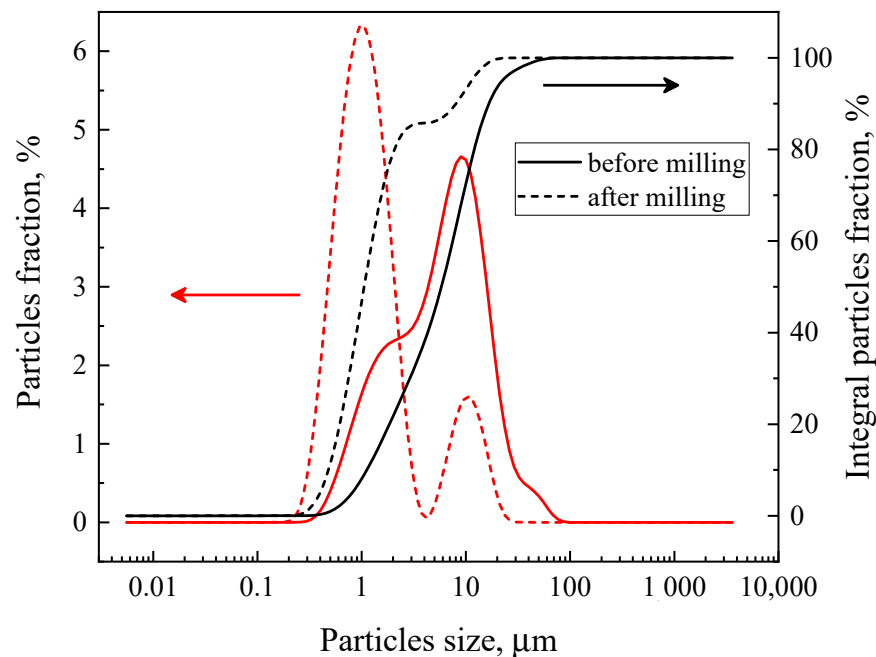
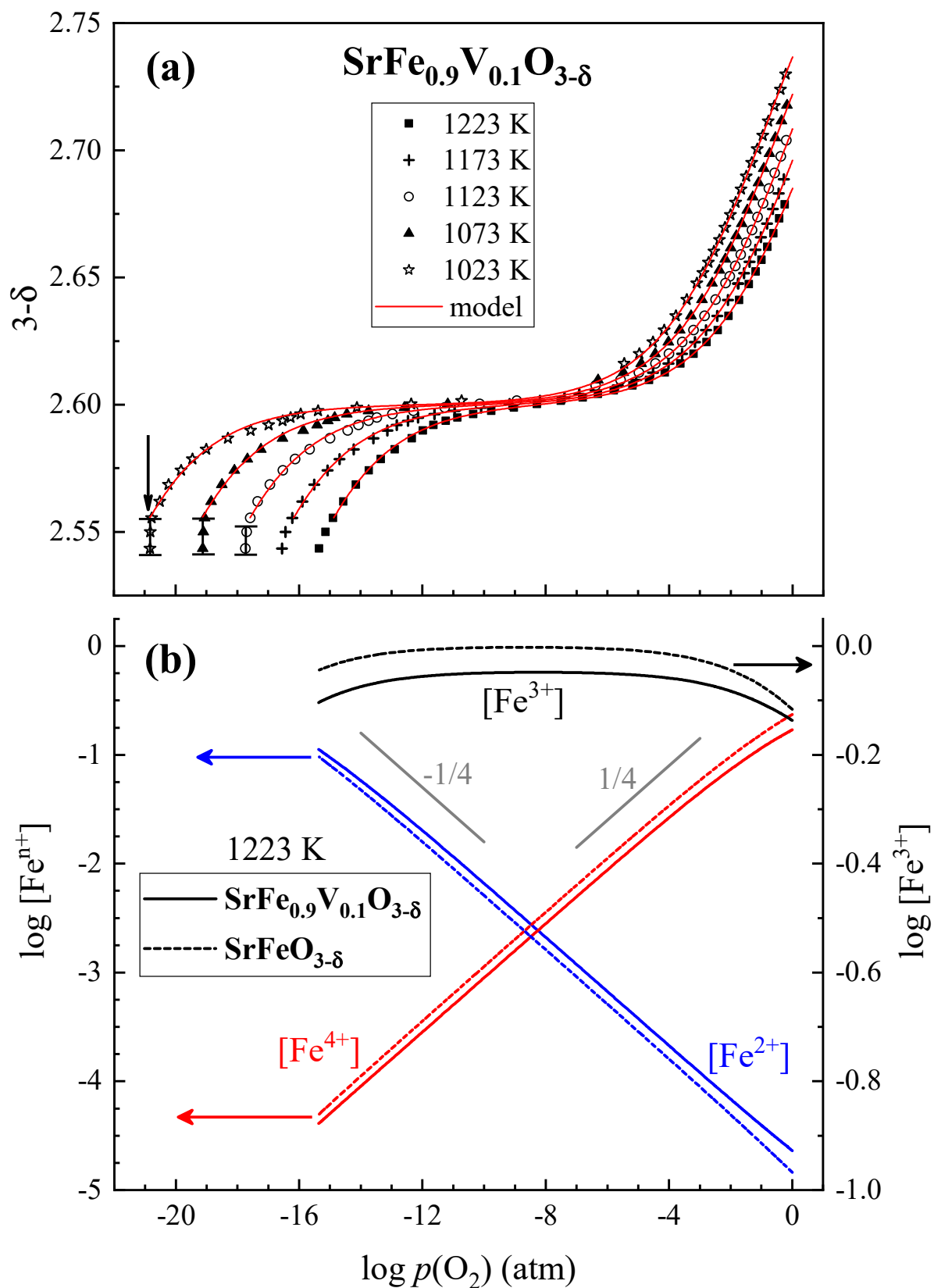


**Figure 3.** Particle size distributions in the initial and ground powders of  $\text{SrFe}_{0.9}\text{V}_{0.1}\text{O}_{3-\delta}$ , determined by the static laser radiation scattering method.

### 3.3. Oxygen Nonstoichiometry and Phase Stability Limit

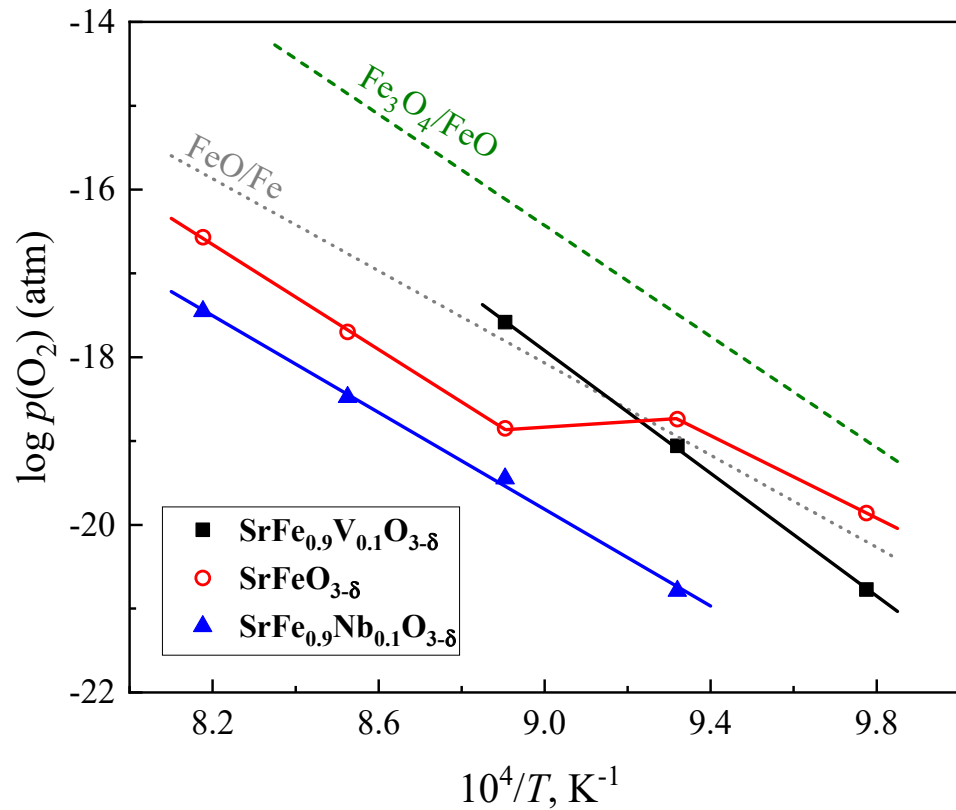
The  $p(\text{O}_2)$ - $T$ - $(3-\delta)$  diagram of  $\text{SrFe}_{0.9}\text{V}_{0.1}\text{O}_{3-\delta}$  (Figure 4a) is typical for most perovskite-type solid solutions based on strontium ferrite [5,26]. In oxidizing atmospheres, the oxygen content decreases with decreasing  $p(\text{O}_2)$  as  $\text{Fe}^{4+}$  states are progressively reduced to  $\text{Fe}^{3+}$ . Then, in the intermediate  $p(\text{O}_2)$  range, the isotherms exhibit inflection points. At lower  $p(\text{O}_2)$ , the oxygen deficiency continues to increase on reduction, which is associated with the appearance of  $\text{Fe}^{2+}$  and, possibly,  $\text{V}^{4+}$  states. The  $p(\text{O}_2)$ - $T$ - $(3-\delta)$  diagram also displays clear indications of perovskite phase decomposition under reducing conditions at 1023–1123 K. The decomposition is reflected by  $p(\text{O}_2)$ -independent variations in the oxygen content, marked by the vertical line segments in Figure 4a. The corresponding oxygen partial pressures can be considered to be the perovskite phase stability limits.

Figure 5 compares the stability boundary of  $\text{SrFe}_{0.9}\text{V}_{0.1}\text{O}_{3-\delta}$  with data from the literature on  $\text{SrFeO}_{3-\delta}$  [4],  $\text{SrFe}_{0.9}\text{Nb}_{0.1}\text{O}_{3-\delta}$  [17] and binary iron oxides [27]. The thermodynamic stability of perovskite-type  $\text{SrFe}_{0.9}\text{V}_{0.1}\text{O}_{3-\delta}$  is moderately higher than that of undoped strontium ferrite at temperatures below 1073 K when the latter possesses a brownmillerite structure. At higher temperatures, when a brownmillerite polymorph transforms into cubic  $\text{SrFeO}_{3-\delta}$  perovskite, the stability of  $\text{SrFe}_{0.9}\text{V}_{0.1}\text{O}_{3-\delta}$  with respect to reductive decomposition is lower. The stability of  $\text{SrFe}_{0.9}\text{V}_{0.1}\text{O}_{3-\delta}$  is also worse than that of the Nb-containing analogue (Figure 5). As mentioned above, the title composition may hardly be used for SOFC anodes and SOEC cathodes. At the same time, its stability under reducing conditions may be improved by the partial substitution of Sr for rare-earth cations.



**Figure 4.** Oxygen partial pressure dependencies of the oxygen content (a) and the calculated concentrations of iron cations in different oxidation states (b). For (a), red solid lines correspond to the fitting results and vertical line segments indicate phase decomposition. The data on  $\text{SrFeO}_{3-\delta}$  [5] are shown for comparison.

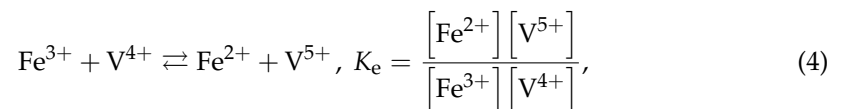
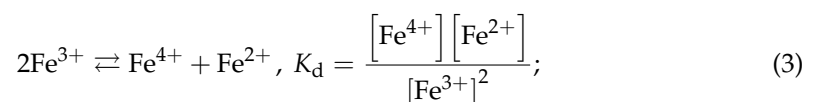
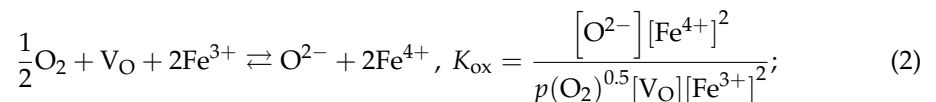




**Figure 5.** Stability limit of SrFe<sub>0.9</sub>V<sub>0.1</sub>O<sub>3-δ</sub> perovskite under reducing conditions. The data on SrFeO<sub>3-δ</sub> [4], SrFe<sub>0.9</sub>Nb<sub>0.1</sub>O<sub>3-δ</sub> [17], and Fe<sub>3</sub>O<sub>4</sub>/FeO and FeO/Fe phase boundaries [27] are shown for comparison.

### 3.4. Point Defect Formation Model

Within the perovskite phase existence domain, the  $p(O_2)$ - $T$ - $(3-\delta)$  diagram of SrFe<sub>0.9</sub>V<sub>0.1</sub>O<sub>3-δ</sub> can be described by a point defect model similar to those used for other SrFeO<sub>3</sub> and La<sub>1-x</sub>Sr<sub>x</sub>FeO<sub>3-δ</sub>-based solid solutions [5,26,28–30]. This model assumes dominant roles for three major defect reactions, namely, iron oxidation (Equation (2)), charge disproportionation of iron cations (Equation (3)), and electron exchange between iron and vanadium ions (Equation (4)):



where  $K_{ox}$ ,  $K_d$  and  $K_e$  are the corresponding equilibrium constants. This model is based on the ideal solution approximation when the standard thermodynamic functions of the reactions (2)–(4) are independent of defect concentrations, leading to the following temperature dependence of all equilibrium constants:

$$K_i = \exp\left(-\frac{\Delta G_i^0}{RT}\right) = \exp\left(-\frac{\Delta H_i^0}{RT} + \frac{\Delta S_i^0}{R}\right), \quad (5)$$

where  $R$  is the gas constant, whereas  $\Delta G_i^0$ ,  $\Delta H_i^0$ ,  $\Delta S_i^0$  are the standard free Gibbs energy, enthalpy and entropy for the defect formation reactions, respectively. The site conservation conditions were formulated as

$$\begin{cases} [\text{Fe}^{2+}] + [\text{Fe}^{3+}] + [\text{Fe}^{4+}] = 0.9 \\ [\text{V}^{4+}] + [\text{V}^{5+}] = 0.1 \end{cases}, \quad (6)$$

$$\begin{cases} [\text{O}^{2-}] = 3 - \delta - \Delta\delta_{\text{ref}} \\ [\text{V}_\text{O}] = \delta - w - \Delta\delta_{\text{ref}} \end{cases}. \quad (7)$$

Equation (7) contains two empirical parameters,  $\Delta\delta_{\text{ref}}$  and  $w$ . The former, reflecting experimental errors, is introduced to correct experimental data on the oxygen content. The  $w$  parameter corresponds to the number of anion sites unavailable for oxygen ions for various physical reasons, such as phenomena related to local ordering and grain boundaries, per formula unit. Finally, the electroneutrality condition can be written as follows:

$$2[\text{Sr}^{2+}] + 2[\text{Fe}^{2+}] + 3[\text{Fe}^{3+}] + 4[\text{Fe}^{4+}] + 4[\text{V}^{4+}] + 5[\text{V}^{5+}] = 2[\text{O}^{2-}]. \quad (8)$$

Solving of Equations (2)–(8) makes it possible to formulate the following final model:

$$5.2 - 0.9 \frac{K_d - K_{\text{ox}} T_s}{K_d + K_{\text{ox}} T_s + \sqrt{K_{\text{ox}} T_s}} - 0.1 \frac{K_d}{K_d + K_e \sqrt{K_{\text{ox}} T_s}} = 2(3 - \delta + \Delta\delta_{\text{ref}}), \quad (9)$$

where  $T_s = \frac{\delta - w - \Delta\delta_{\text{ref}}}{3 - \delta + \Delta\delta_{\text{ref}}} \cdot \sqrt{p(\text{O}_2)}$ . The Levenberg–Marquardt algorithm of the LMFIT library [31] was used for fitting Equation (9) to the experimental data.

Preliminary calculations demonstrated that the thermodynamic parameters of the electron exchange reaction between iron and vanadium ( $\Delta H_e^0$  and  $\Delta S_e^0$ ) have high rates of error, whilst their variations have no effect on the fitting results. Therefore, the model was simplified by excluding Equation (4). In other words, the presence of  $\text{V}^{4+}$  was neglected in Equations (6) and (8);  $\text{V}^{5+}$  concentration was assumed to be constant and equal to 0.1.

The fitting results using this model (red solid lines in Figure 4a) well describe the experimental data. Table 1 compares the thermodynamic parameters calculated for  $\text{SrFe}_{0.9}\text{V}_{0.1}\text{O}_{3-\delta}$  and those for similar materials reported elsewhere. Within the uncertainty limits, thermodynamic functions of the oxidation and iron disproportionation reactions are similar for all presented compositions, except for undoped  $\text{SrFeO}_{3-\delta}$ .

**Table 1.** Thermodynamic parameters (\*) of the defect formation reactions in  $\text{SrFe}_{0.9}\text{V}_{0.1}\text{O}_{3-\delta}$  and other strontium ferrite-based phases.

Composition	$\Delta H_{\text{ox}}^0$ , kJ·mol <sup>-1</sup>	$\Delta S_{\text{ox}}^0$ , J·mol <sup>-1</sup> ·K <sup>-1</sup>	$\Delta H_{\text{d}}^0$ , kJ·mol <sup>-1</sup>	$\Delta S_{\text{d}}^0$ , J·mol <sup>-1</sup> ·K <sup>-1</sup>	$w$	Ref.
$\text{SrFe}_{0.9}\text{V}_{0.1}\text{O}_{3-\delta}$	$-98.4 \pm 0.6$	$-78.2 \pm 0.5$	$129 \pm 1$	$7.5 \pm 0.5$	$0.203 \pm 0.001$	this work
$\text{SrFe}_{0.93}\text{Mo}_{0.07}\text{O}_{3-\delta}$	$-94 \pm 3$	$-80 \pm 2$	$132 \pm 3$	$7 \pm 2$	-	[5]
$\text{SrFeO}_{3-\delta}$	$-102 \pm 6$	$-87 \pm 5$	$122.5 \pm 0.2$	0 **	-	[5]

\* The temperature ranges used for the calculations were 1023–1223 K for  $\text{SrFe}_{0.9}\text{V}_{0.1}\text{O}_{3-\delta}$ , 1073–1223 K for  $\text{SrFe}_{0.93}\text{Mo}_{0.07}\text{O}_{3-\delta}$  and 1148–1223 K for  $\text{SrFeO}_{3-\delta}$ . \*\* Statistically insignificant.

### 3.5. Defect Concentrations and Oxygen Thermodynamic Functions

The obtained thermodynamic parameters were used to calculate concentrations of iron states as a function of  $p(\text{O}_2)$ . As an example, Figure 4b compares the variations for  $\text{SrFe}_{0.9}\text{V}_{0.1}\text{O}_{3-\delta}$  and  $\text{SrFeO}_{3-\delta}$  at 1223 K. Under moderately oxidizing and reducing conditions, the concentrations of  $\text{Fe}^{2+}$  and  $\text{Fe}^{4+}$  are proportional to  $p(\text{O}_2)^{\pm 1/4}$ . At high

oxygen pressures, when the average oxidation state of iron cations is far from 3+, a deviation from the power law is observed. The calculations showed that the introduction of vanadium into the iron sublattice of  $\text{SrFeO}_{3-\delta}$  increases  $\text{Fe}^{2+}$  content and decreases  $\text{Fe}^{4+}$  concentration with respect to undoped ferrite.

The experimental  $p(\text{O}_2)$ - $T$ -( $3-\delta$ ) diagram was then used to calculate the increments of oxygen chemical potential ( $\Delta\mu_{\text{O}}$ ):

$$\Delta\mu_{\text{O}} = \frac{1}{2}RT \ln p(\text{O}_2). \quad (10)$$

As the dependence of  $\Delta\mu_{\text{O}}$  on temperature at fixed ( $3-\delta$ ) values is linear, the partial molar enthalpy ( $\Delta h_{\text{O}}$ ) and entropy ( $\Delta s_{\text{O}}$ ) of oxygen incorporation in the lattice can be extracted:

$$\Delta\mu_{\text{O}} = \Delta h_{\text{O}} - T\Delta s_{\text{O}}. \quad (11)$$

The calculated values of the partial molar thermodynamic functions of oxygen are shown by dots in Figure 6a,b). Their dependencies on the oxygen vacancy concentration are non-monotonic and have breakpoints at  $(3-\delta) \approx 2.6$  associated with changing dominant mechanisms of the defect formation, as discussed below. The partial molar enthalpy is almost constant before and after its breakpoint (Figure 6a), thus confirming the applicability of the ideal solution approximation. It should be noted, however, that this approximation may not always be applicable in complex oxide systems, especially in systems involving multiple cations and substantial variations in oxygen nonstoichiometry. For instance, a deviation from the ideal solution behavior in undoped  $\text{SrFeO}_{3-\delta}$  is observed near  $\delta = 0.5$ , reflected by a decrease in the partial molar entropy of oxygen due to the vacancy ordering [32].

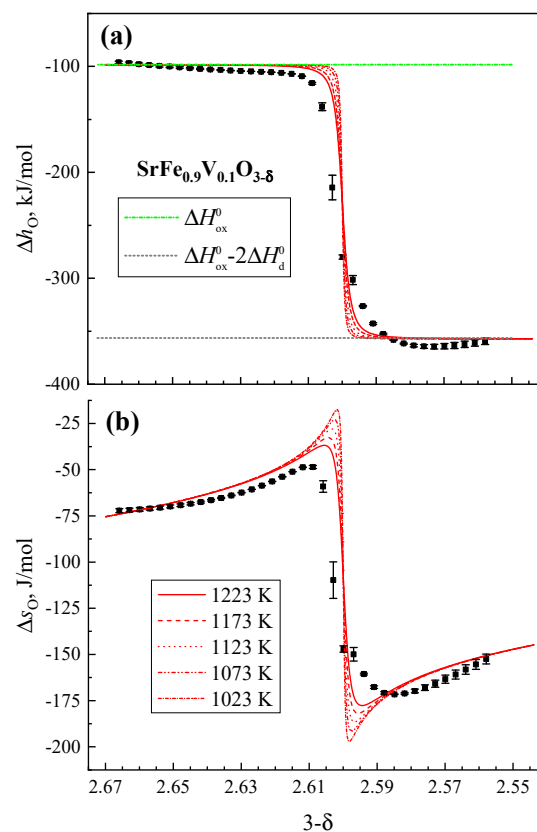


**Figure 6.** Partial molar enthalpy (a) and entropy (b) of oxygen as functions of the oxygen content in  $\text{SrFe}_{0.9}\text{V}_{0.1}\text{O}_{3-\delta}$ . Dots present the results obtained using the Gibbs–Helmholtz relationship. Red lines show the results of statistical thermodynamic modeling.

### 3.6. Statistical Thermodynamic Modeling

In order to additionally verify the adequacy of the calculated thermodynamic parameters listed in Table 1, these were used for statistical thermodynamic modeling of the partial molar enthalpy and entropy. The modeling results were then compared to the quantities directly extracted from the experimental  $p(\text{O}_2)$ - $T$ -( $3-\delta$ ) diagram.

Using the ideal solution approximation and assuming statistical distribution of all defect species in the corresponding sublattices, the total Gibbs energy for  $\text{SrFe}_{0.9}\text{V}_{0.1}\text{O}_{3-\delta}$  is determined as [30]

$$G = G^0 + [\text{Sr}^{2+}] \mu_{\text{Sr}^{2+}}^0 + [\text{Fe}^{2+}] \mu_{\text{Fe}^{2+}}^0 + [\text{Fe}^{3+}] \mu_{\text{Fe}^{3+}}^0 + [\text{Fe}^{4+}] \mu_{\text{Fe}^{4+}}^0 + [\text{V}^{5+}] \mu_{\text{V}^{5+}}^0 + (3-\delta) \mu_{\text{O}^{2-}}^0 + \delta \mu_{\text{V}_\text{O}}^0 - T \cdot S_{\text{conf}}, \quad (12)$$

where  $G^0$  is the standard Gibbs energy and  $S_{\text{conf}}$  is the total configurational entropy. The latter quantity in the Stirling approximation is defined by the formula [33]

$$S_{\text{conf}} = -R \cdot \sum_i x_i \ln(x_i), \quad (13)$$

where  $x_i$  is the concentration of  $i$ -th component ( $\text{Sr}^{2+}$ ,  $\text{Fe}^{2+}$ ,  $\text{Fe}^{3+}$ ,  $\text{Fe}^{4+}$ ,  $\text{V}^{5+}$ ,  $\text{O}^{2-}$ ,  $\text{V}_\text{O}$ ). The chemical potential of oxygen can be determined as

$$\mu_{\text{O}} = \frac{\partial G}{\partial [\text{O}^{2-}]} = \frac{\partial G}{\partial (3-\delta)} = -\frac{\partial G}{\partial \delta} = -\frac{\partial [\text{Fe}^{2+}]}{\partial \delta} \cdot \mu_{\text{Fe}^{2+}}^0 - \frac{\partial [\text{Fe}^{3+}]}{\partial \delta} \cdot \mu_{\text{Fe}^{3+}}^0 - \frac{\partial [\text{Fe}^{4+}]}{\partial \delta} \cdot \mu_{\text{Fe}^{4+}}^0 + \mu_{\text{O}^{2-}}^0 - \mu_{\text{V}_\text{O}}^0 - T \cdot s_{\text{O conf}}, \quad (14)$$

$$s_{\text{O conf}} = -\frac{\partial S_{\text{conf}}}{\partial \delta}. \quad (15)$$

Using Equations (2)–(8) and (13)–(15), one can obtain

$$\Delta \mu_{\text{O}} = (\Delta G_{\text{ox}}^0 - 2 \cdot \Delta G_{\text{d}}^0) - \frac{\partial [\text{Fe}^{4+}]}{\partial \delta} \cdot \Delta G_{\text{d}}^0 - T \cdot s_{\text{O conf}}, \quad (16)$$

$$\Delta h_{\text{O}} = (\Delta H_{\text{ox}}^0 - 2 \cdot \Delta H_{\text{d}}^0) - \frac{\partial [\text{Fe}^{4+}]}{\partial \delta} \cdot \Delta H_{\text{d}}^0, \quad (17)$$

$$\Delta s_{\text{O}} = (\Delta S_{\text{ox}}^0 - 2 \cdot \Delta S_{\text{d}}^0) - \frac{\partial [\text{Fe}^{4+}]}{\partial \delta} \cdot \Delta S_{\text{d}}^0 + s_{\text{O conf}}, \quad (18)$$

$$s_{\text{O conf}} = R \left( \frac{\partial [\text{Fe}^{4+}]}{\partial \delta} \cdot \ln(K_{\text{d}}) + \ln \left( \frac{K_{\text{d}}^2}{K_{\text{ox}} \cdot \sqrt{p_{\text{O}_2}}} \right) \right). \quad (19)$$

For the concentrations of  $\text{Fe}^{2+}$ ,  $\text{Fe}^{3+}$ ,  $\text{Fe}^{4+}$ , oxygen ions and vacancies

$$[\text{Fe}^{2+}] = \frac{0.9 \cdot K_{\text{d}}}{K_{\text{ox}} T_{\text{s}} + \sqrt{K_{\text{ox}} T_{\text{s}}} + K_{\text{d}}}, \quad (20)$$

$$[\text{Fe}^{3+}] = \frac{0.9 \cdot \sqrt{K_{\text{ox}} T_{\text{s}}}}{K_{\text{ox}} T_{\text{s}} + \sqrt{K_{\text{ox}} T_{\text{s}}} + K_{\text{d}}}, \quad (21)$$

$$[\text{Fe}^{4+}] = \frac{0.9 \cdot K_{\text{ox}} T_{\text{s}}}{K_{\text{ox}} T_{\text{s}} + \sqrt{K_{\text{ox}} T_{\text{s}}} + K_{\text{d}}}, \quad (22)$$

$$[\text{O}^{2-}] = 3 - \delta - \Delta \delta_{\text{ref}}, \quad (23)$$

$$[\text{V}_\text{O}] = \delta - w - \Delta \delta_{\text{ref}}. \quad (24)$$

The results of the statistical thermodynamic modeling are shown in Figure 6a,b by red lines. Notice that, at high oxygen content in  $\text{SrFe}_{0.9}\text{V}_{0.1}\text{O}_{3-\delta}$ , the partial molar enthalpy

of oxygen corresponds well to the enthalpy of the  $\text{Fe}^{3+}$  oxidation reaction (Equation (2)). After the breakpoint,  $\Delta h_{\text{O}}$  decreases down to the enthalpy of  $\text{Fe}^{2+}$  oxidation ( $\Delta H_{\text{ox}}^0 - 2\Delta H_{\text{d}}^0$ ) in accordance with the reaction  $\frac{1}{2}\text{O}_2 + \text{V}_{\text{O}} + 2\text{Fe}^{2+} \rightleftharpoons \text{O}^{2-} + 2\text{Fe}^{3+}$ . The corresponding levels are shown in Figure 6a by the horizontal dashed lines. This agreement further validates the proposed point defect model.

### 3.7. Nonstoichiometry and Tolerance Factor at Room Temperature

According to TGA results (Figure S2),  $\text{SrFe}_{0.9}\text{V}_{0.1}\text{O}_{3-\delta}$  remains oxygen deficient at room temperature when the oxygen content is approximately 2.8. This corresponds to the average oxidation state of iron-site cations of +3.6. As all vanadium in these conditions is pentavalent, the concentrations of  $\text{Fe}^{3+}$  and  $\text{Fe}^{4+}$  per formula unit are equal to 0.5 and 0.4, respectively. One may calculate the Goldschmidt tolerance factor [34] as follows:

$$t = \frac{r_{\text{A}} + r_{\text{O}^{2-}}}{\sqrt{2}(r_{\text{B}} + r_{\text{O}^{2-}})} \quad (25)$$

where  $r_{\text{A}}$  and  $r_{\text{B}}$  are the average radii of A- and B-cations, respectively, and  $r_{\text{O}^{2-}}$  is the radius of oxygen anions. The data on ionic radii [35] provide a value of  $t = 1.006$ , which corresponds to the stability criterion for cubic perovskite structures [34]. Note that even a slightly larger  $t$  value would lead to structural instability, thus explaining why the solid solution formation limit in an  $\text{SrFe}_{1-x}\text{V}_x\text{O}_{3-\delta}$  system corresponds approximately to  $x = 0.1$ .

### 3.8. Lattice Expansion and Electrical Conductivity

The dilatometric curve of  $\text{SrFe}_{0.9}\text{V}_{0.1}\text{O}_{3-\delta}$  ceramics, recorded in the dynamic mode in air, exhibits two linear parts with a transition at 780 K when extensive oxygen losses with increasing temperature start (Figure 7). In the low-temperature range, the TEC is equal to  $(14.2 \pm 0.1) \times 10^{-6} \text{ K}^{-1}$  (Table 2). This value reflects mainly thermal-induced lattice expansion. At higher temperatures, the apparent TEC increases up to  $(24.8 \pm 0.1) \times 10^{-6} \text{ K}^{-1}$  due to the chemical contribution associated with a decreasing iron oxidation state. Within the limits of experimental uncertainties, the latter value is equal to that obtained using the static regime with isothermal dwells for equilibration at 873–1273 K. During isothermal reduction in flowing argon, an increase in chemical expansion with decreasing temperature is observed (Figure 8a). This behavior well correlates with the oxygen nonstoichiometry variations (Figure 4a). As a consequence, the  $\varepsilon_{\text{chem}}/\Delta\delta$  coefficient (so-called chemical expansivity) is almost independent of temperature (Figure 8b). Another necessary comment is that the chemical expansion of  $\text{SrFe}_{0.9}\text{V}_{0.1}\text{O}_{3-\delta}$  ceramics is moderate with respect to other ferrite-based mixed conductors considered to be promising electrode materials (e.g., [36]). For the sake of comparison, Figure 8a displays analogous data on  $\text{La}_{0.5}\text{Sr}_{0.5}\text{Fe}_{0.5}\text{Co}_{0.5}\text{O}_{3-\delta}$  [36] and  $\text{Sr}_{0.97}\text{Fe}_{0.7}\text{Al}_{0.2}\text{Mo}_{0.1}\text{O}_{3-\delta}$  [37] perovskites.

The average TEC of  $\text{SrFe}_{0.9}\text{V}_{0.1}\text{O}_{3-\delta}$  ceramics in an argon atmosphere is lower than that in air (Table 2), again in correlation with the  $p(\text{O}_2)$ - $T$ -( $3-\delta$ ) diagram. Notice that, at elevated temperatures, the average TEC of  $\text{SrFeO}_{3-\delta}$  is as high as  $(33\text{--}34) \times 10^{-6} \text{ K}^{-1}$  [3,8]. Therefore, doping with 10% vanadium makes it possible to improve thermomechanical properties, a result of a lower oxygen deficiency and lower iron oxidation state in  $\text{SrFe}_{0.9}\text{V}_{0.1}\text{O}_{3-\delta}$  compared to  $\text{SrFeO}_{3-\delta}$  (Figure S2). In addition, the TEC of  $\text{SrFe}_{0.9}\text{V}_{0.1}\text{O}_{3-\delta}$  is also lower than those for other 10% B-site-doped ferrites, such as  $\text{SrFe}_{0.9}\text{Nb}_{0.1}\text{O}_{3-\delta}$  and  $\text{SrFe}_{0.9}\text{Ta}_{0.1}\text{O}_{3-\delta}$  (Table 2). At the same time, the expansion of  $\text{SrFe}_{0.9}\text{V}_{0.1}\text{O}_{3-\delta}$  in the high temperature range is still larger compared to most SOFC electrolytes based on zirconia, ceria and lanthanum gallate [8]. The chemical contribution to the lattice expansion may have a negative impact on the long-term stability of the electrodes under current and temperature variations, inducing disruptions in the mechanical integrity.

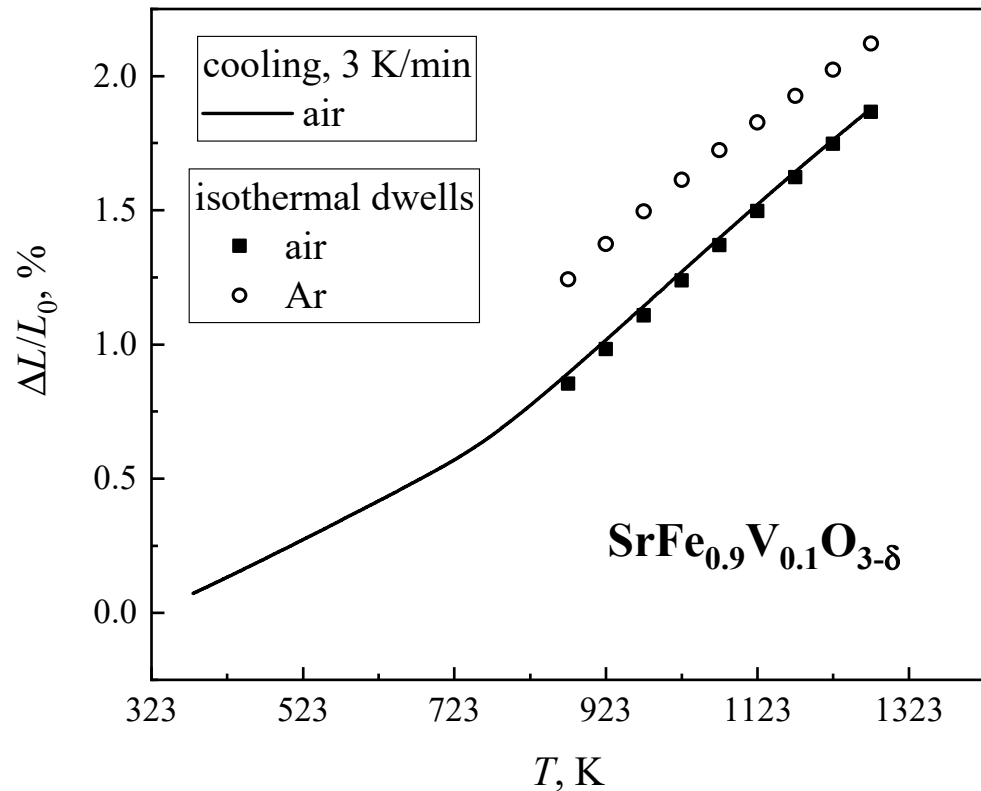


**Figure 7.** Temperature dependencies of the relative elongations of  $\text{SrFe}_{0.9}\text{V}_{0.1}\text{O}_{3-\delta}$  ceramics, collected in the regimes of continuous cooling and isothermal dwells.

**Table 2.** Apparent TECs of  $\text{SrFeO}_{3-\delta}$ -based materials.

Composition	Atmosphere	Conditions	$T$ , K	$\text{TEC} \times 10^6$ , $\text{K}^{-1}$	Ref.
$\text{SrFe}_{0.9}\text{V}_{0.1}\text{O}_{3-\delta}$	air	isothermal dwells	873–1273	$25.0 \pm 0.3$	This work
		cooling, 3 K/min	873–1273	$24.8 \pm 0.1$	
	Ar *	isothermal dwells	373–673	$14.2 \pm 0.1$	
			873–1273	$22 \pm 1$	
$\text{SrFe}_{0.9}\text{Nb}_{0.1}\text{O}_{3-\delta}$	air	heating, 5 K/min	683–1273	27.5	[16]
			300–683	15.6	
$\text{SrFe}_{0.9}\text{Ta}_{0.1}\text{O}_{3-\delta}$	air	heating	823–1173	37.0	[18]
			300–823	14.8	
$\text{SrFeO}_{3-\delta}$	air	heating, 2 K/min	623–1373	34.1	[3]
			323–523	15.6	

\*  $p(\text{O}_2) = 7.6 \times 10^{-5}$  atm.

The temperature dependencies of total electrical conductivity (Figure 9) also exhibit a behavior typical for perovskite-like ferrites [4,7], where the appearance of maxima at 600–800 K is associated with the progressive release of oxygen from the crystal lattice at high temperatures, as discussed above. The observed decrease in conductivity on heating appears due to the dominant role of  $p$ -type electronic charge carriers, the concentration of which decreases with increasing oxygen nonstoichiometry. As  $p(\text{O}_2)$  decreases, the number of oxygen vacancies increases and the concentration of electron holes becomes lower (Figure 4a,b). One should separately mention that the incorporation of vanadium in  $\text{SrFeO}_{3-\delta}$  reduces the concentration of  $\text{Fe}^{4+}$  and  $\text{Fe}^{3+}$  states involved in the  $p$ -type electronic transport (Figure 4b). Moreover, the presence of relatively stable  $\text{V}^{5+}$  in the iron sublattice leads to a lower concentration of Fe-O-Fe bonds responsible for the electron transfer. Note

also that  $V^{5+}$  has a smaller ionic radius (0.54 Å) than  $Fe^{3+}$  (0.645 Å) [35], which can lead to local lattice distortions. As a result, a moderate decrease in electrical conductivity and an increase in its activation energy at temperatures below 700 K are observed when vanadium is substituted for iron (Figure 9). In the case of  $SrFe_{0.9}V_{0.1}O_{3-\delta}$ , the apparent activation energy for the conductivity in the low-temperature range is  $21 \pm 2$  kJ/mol in air and  $26 \pm 1$  kJ/mol in an argon atmosphere. At the same time, the conductivity of V-substituted  $SrFeO_{3-\delta}$  is higher compared to Ta-doped  $SrFeO_{3-\delta}$  and is nearly equal to that of  $SrFe_{0.9}Nb_{0.1}O_{3-\delta}$  at elevated temperatures (Figure 9).

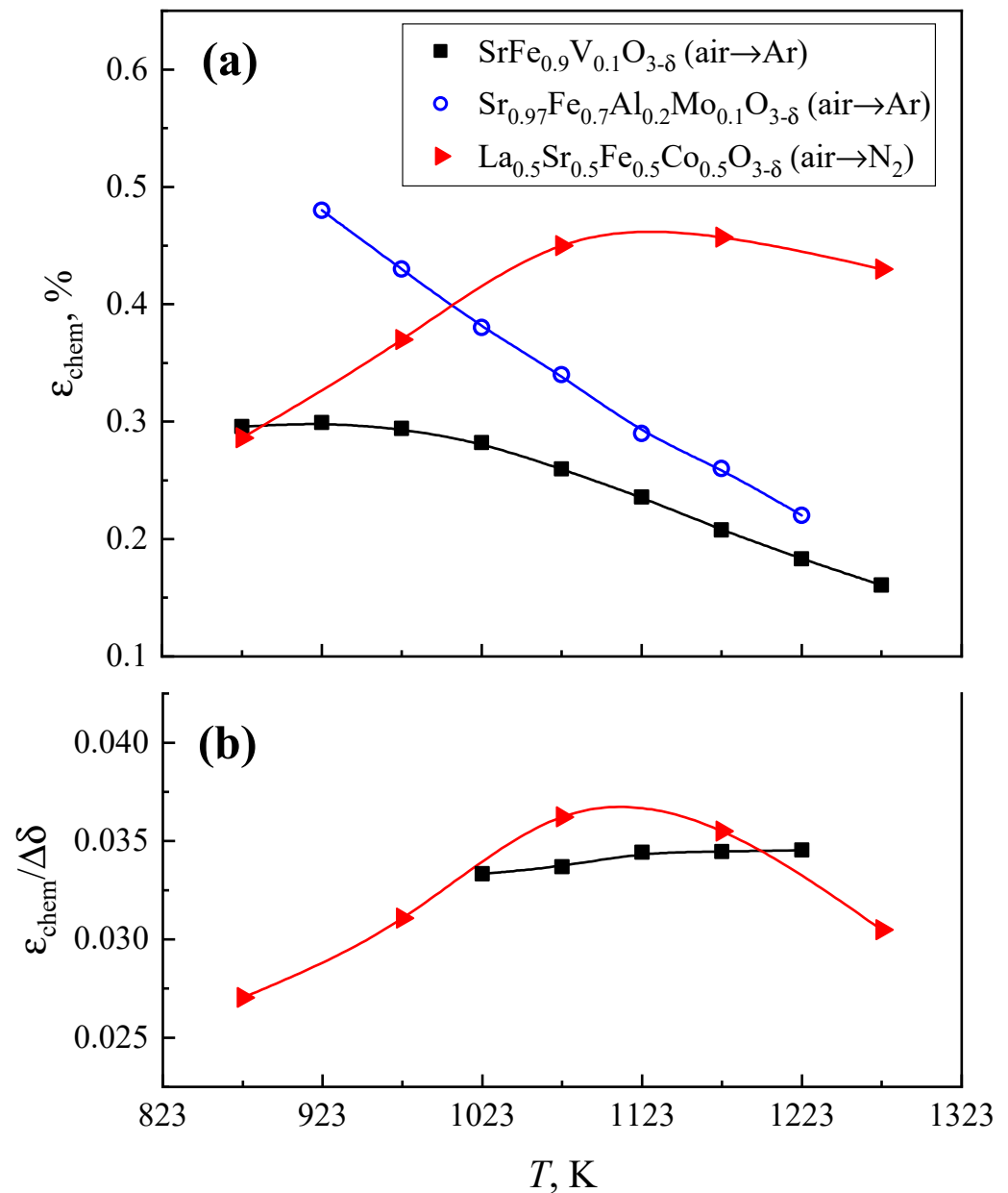


**Figure 8.** Temperature dependencies of the chemical expansion on isothermal reduction (a) and  $\epsilon_{chem}/\Delta\delta$  coefficient (b) for  $SrFe_{0.9}V_{0.1}O_{3-\delta}$  ceramics. Data on  $La_{0.5}Sr_{0.5}Fe_{0.5}Co_{0.5}O_{3-\delta}$  [36] and  $Sr_{0.97}Fe_{0.7}Al_{0.2}Mo_{0.1}O_{3-\delta}$  [37] are shown for comparison.

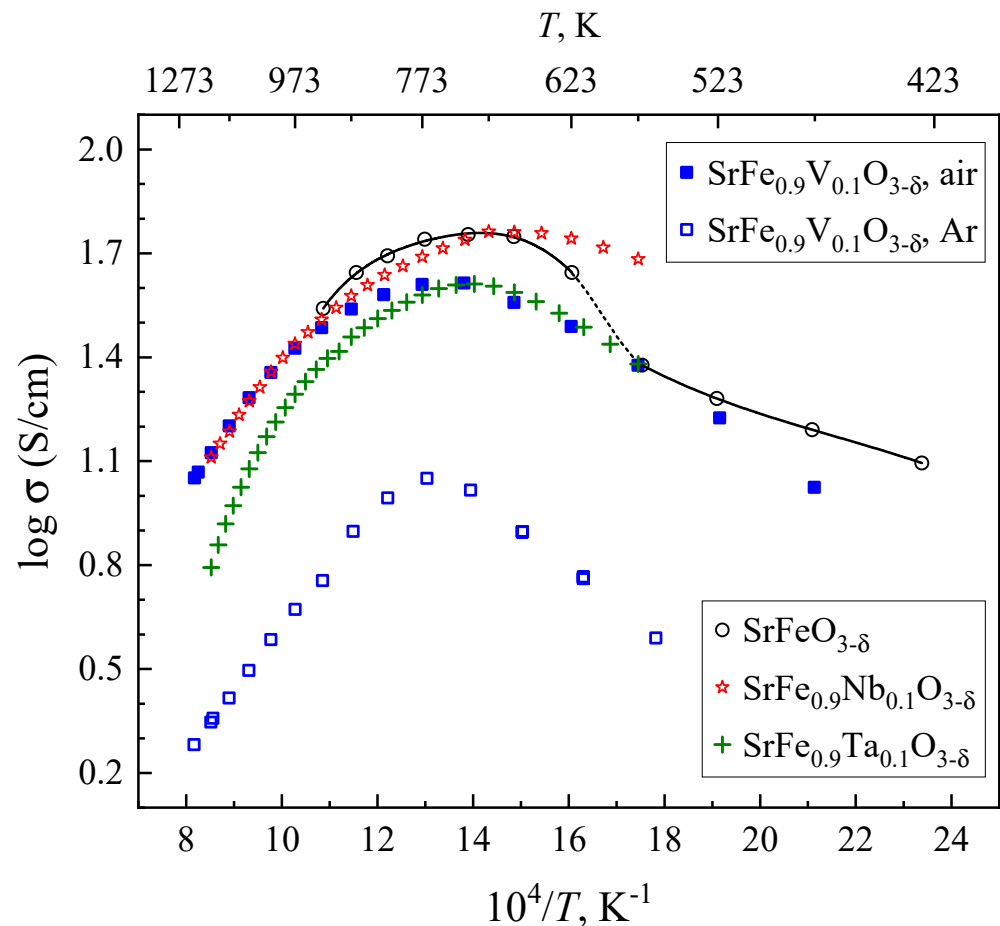


**Figure 9.** Temperature dependencies of the total electrical conductivity of  $\text{SrFe}_{0.9}\text{V}_{0.1}\text{O}_{3-\delta}$  ceramics. Data on  $\text{SrFeO}_{3-\delta}$  [38],  $\text{SrFe}_{0.9}\text{Nb}_{0.1}\text{O}_{3-\delta}$  [16] and  $\text{SrFe}_{0.9}\text{Ta}_{0.1}\text{O}_{3-\delta}$  [19] in air are shown for the sake of comparison.

### 3.9. Electrode Behavior

In order to simulate the operating conditions in SOFC cathodes and SOEC anodes, the electrochemical activity of  $\text{SrFe}_{0.9}\text{V}_{0.1}\text{O}_{3-\delta}$  electrodes was tested under current loads in both directions. The polarization curves (Figure 10) exhibit nonlinear behavior; the anodic overpotentials are slightly lower than the absolute values of the cathodic ones. This trend can be explained by increasing oxygen chemical potential at the WE surface under anodic polarization with respect to equilibrium. Such an increase results in a higher concentration of electron holes and electrical conductivity. Cathodic polarization has the opposite effect. These differences mean that the  $\text{SrFe}_{0.9}\text{V}_{0.1}\text{O}_{3-\delta}$  electrode demonstrates higher electrochemical activity in electrolysis mode compared to the fuel cell regime. Despite the differences in anodic and cathodic kinetics, the entire polarization curves can be satisfactorily described by the Butler–Volmer equation [39]:

$$i = i_0 \left[ \exp\left(\frac{\alpha n F \eta}{RT}\right) - \exp\left(-\frac{\beta n F \eta}{RT}\right) \right], \quad (26)$$

where  $n$  is the number of electrons participating in the rate-determining step,  $\alpha$  and  $\beta$  are the charge transfer coefficients and  $i_0$  is the exchange current density. One example of the fitting results using this equation is presented in Figure 10b. The calculated  $i_0$  value is  $35 \pm 5 \text{ mA/cm}^2$ .



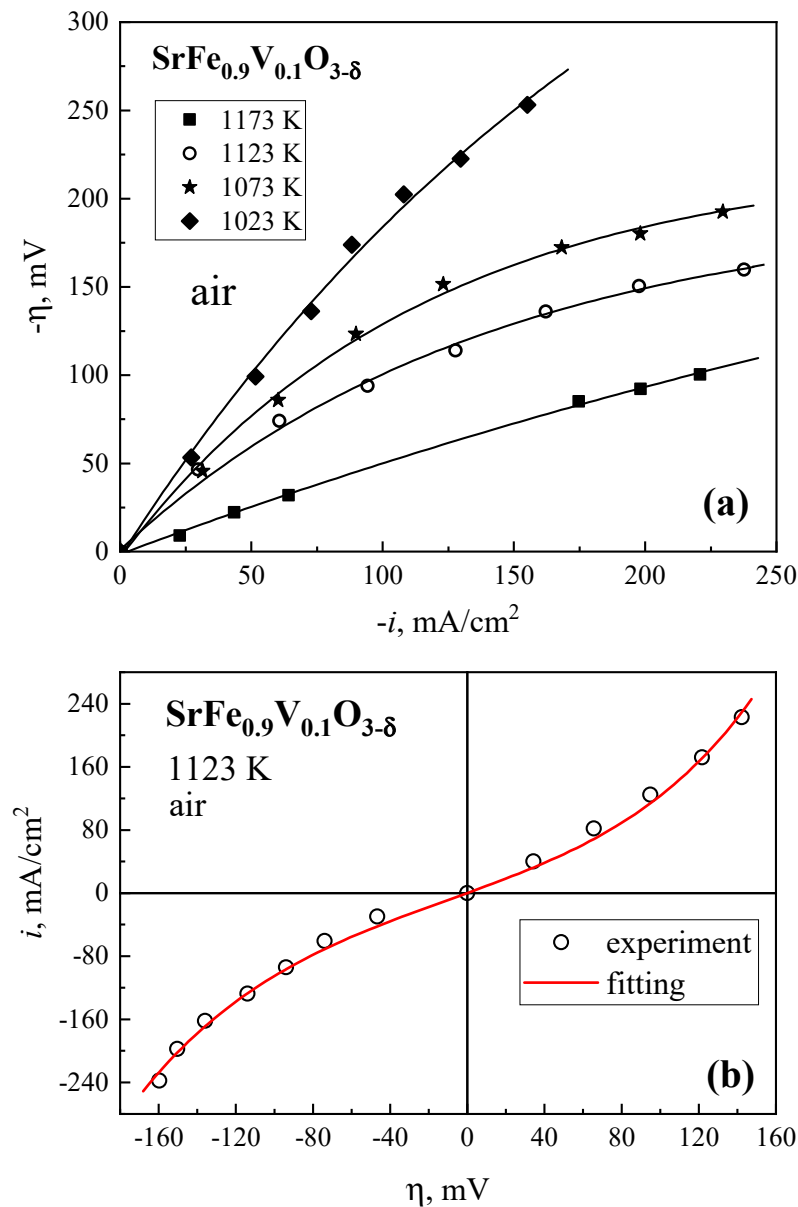


**Figure 10.** Current density dependencies of the cathodic overpotentials of a porous  $\text{SrFe}_{0.9}\text{V}_{0.1}\text{O}_{3-\delta}$  electrode in air at 1023–1173 K (a) and of the cathodic and anodic overpotentials at 1123 K (b). For (b), red solid line shows fitting results.

The impedance spectra consist of two separable arcs, which were modeled by two sequential processes (Figure 11a). The high-frequency signal was attributed to the charge transfer process, whilst the signal at low frequencies relates to diffusion phenomena. At the cathodic current density of  $-128 \text{ mA/cm}^2$ , the overpotential is approximately  $-114 \text{ mV}$  at 1123 K. Under the open-circuit conditions, the activation energy for reciprocal electrode polarization resistance is  $130 \pm 9 \text{ kJ/mol}$  (Figure 11b), very close to that obtained for  $\text{SrFe}_{0.9}\text{Nb}_{0.1}\text{O}_{3-\delta}$  [16]. This value is typical for the activation energies of oxygen reduction reactions and oxygen diffusion coefficients in  $\text{La}_{1-x}\text{Sr}_x\text{Fe}_{1-y}\text{Co}_y\text{O}_{3-\delta}$  electrodes ([40,41] and references therein). The electrochemical activity of the  $\text{SrFe}_{0.9}\text{V}_{0.1}\text{O}_{3-\delta}$  electrode is higher compared to a number of its analogues based on perovskite-type ferrite and chromite, in particular  $\text{La}_{0.45}\text{Ce}_{0.05}\text{Sr}_{0.5}\text{FeO}_{3-\delta}$  and  $(\text{La}_{0.75}\text{Sr}_{0.25})_{0.95}\text{Cr}_{0.5}\text{Mn}_{0.5}\text{O}_{3-\delta}$  studied under similar conditions [25,26]. For further improvement in the electrochemical activity, microstructural optimization and surface modification of the electrodes are necessary in order to increase exchange currents and conductivity.

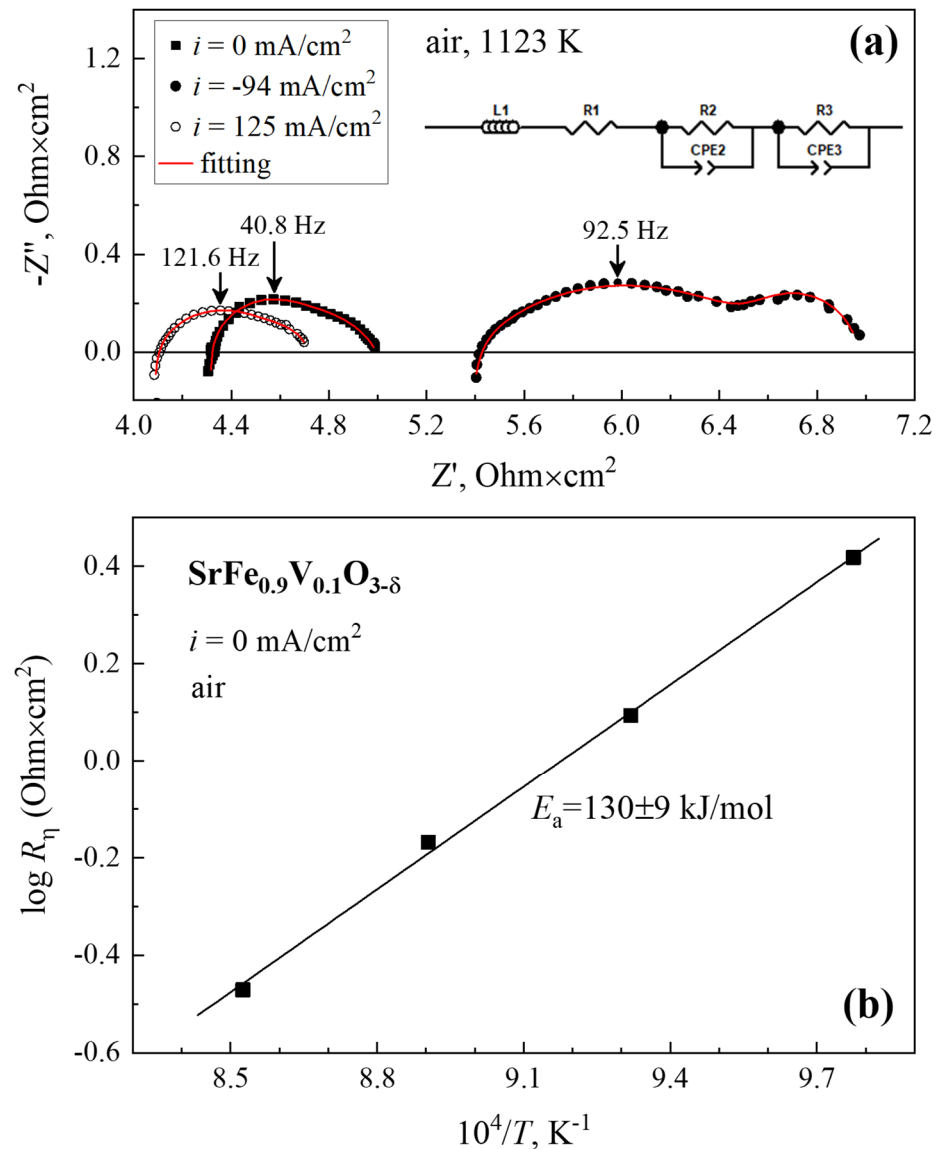


**Figure 11.** Examples of the impedance spectra for a porous  $\text{SrFe}_{0.9}\text{V}_{0.1}\text{O}_{3-\delta}$  electrode (a) and temperature dependence of the area-specific polarization resistance under open-circuit conditions (b).

#### 4. Conclusions

XRD analysis of a perovskite-like  $\text{SrFe}_{1-x}\text{V}_x\text{O}_{3-\delta}$  system showed that the maximum solid solubility of vanadium at atmospheric oxygen pressure corresponds to approximately 10% iron sites. The Goldschmidt tolerance factor of  $\text{SrFe}_{0.9}\text{V}_{0.1}\text{O}_{3-\delta}$ , calculated accounting for the oxidation states of the transition metal cations at room temperature in air, is close to unity. Consequently, this phase possesses a cubic perovskite structure (SG  $Pm\bar{3}m$ ). The  $p(\text{O}_2)$ - $T$ - $(3-\delta)$  diagram of  $\text{SrFe}_{0.9}\text{V}_{0.1}\text{O}_{3-\delta}$  in the oxygen partial pressure range from  $10^{-21}$  to 0.5 atm at 1023–1223 K can be described by an ideal solution model neglecting any reduction of pentavalent  $\text{V}^{5+}$  cations within the phase stability limits. This hypothesis was further confirmed by statistical thermodynamic modeling. If compared to undoped  $\text{SrFeO}_{3-\delta}$ , the substitution with vanadium leads both to lowering oxygen vacancy concentrations and to decreasing average oxidation states of iron cations. These effects are, in turn, responsible for the observed decrease in  $p$ -type electronic conductivity, average TECs, and chemical expansion induced by the oxygen nonstoichiometry variations. Porous  $\text{SrFe}_{0.9}\text{V}_{0.1}\text{O}_{3-\delta}$  electrodes exhibit relatively good electrochemical activity under oxidizing conditions, which is higher with respect to a number of ferrite- and chromite-based electrode materials.

The electrochemical behavior of  $\text{SrFe}_{0.9}\text{V}_{0.1}\text{O}_{3-\delta}$  electrodes suggests the possible relevance of electronic conduction as a polarization resistance-affecting factor.

**Supplementary Materials:** The following supporting information can be downloaded at <https://www.mdpi.com/article/10.3390/ma18030493/s1>, Figure S1: Illustration of the static regime of the dilatometric measurements in flowing air and Ar on temperature cycling at 873–1273 K with equilibration at each temperature; Figure S2: Oxygen content in  $\text{SrFe}_{0.9}\text{V}_{0.1}\text{O}_{3-\delta}$  as a function of temperature in air. Data on  $\text{SrFeO}_{3-\delta}$  [5] and  $\text{SrFe}_{0.9}\text{Nb}_{0.1}\text{O}_{3-\delta}$  [42] are shown for the sake of comparison.

**Author Contributions:** Conceptualization, V.V.K. (Vladislav V. Kharton); methodology, M.V.P.; validation, I.I.Z. and V.V.K. (Victor V. Kedrov); investigation, A.I.I., S.S.N., M.S.D., E.V.T., M.V.P., D.A.A., I.I.Z. and A.O.Z.; data curation, A.I.I., S.S.N., M.S.D., D.A.A. and A.O.Z.; writing—original draft preparation, A.I.I., S.S.N. and V.V.K. (Vladislav V. Kharton); writing—review and editing, S.S.N., E.V.T. and M.V.P.; supervision, V.V.K. (Victor V. Kedrov) and V.V.K. (Vladislav V. Kharton). All authors have read and agreed to the published version of the manuscript.

**Funding:** The work was partly supported within the framework of the state task of ISSP RAS.

**Data Availability Statement:** The original contributions presented in the study are included in the article, further inquiries can be directed to the corresponding authors.

**Acknowledgments:** Equipment from the Scientific Facility Center, Osipyan Institute of Solid State Physics RAS, was used in this work. The work was partly supported within the framework of the state task of ISSP RAS.

**Conflicts of Interest:** The authors declare no conflict of interest.

## Nomenclature

### List of abbreviations

10Sc1YSZ	10 mol.% scandia- and 1 mol.% yttria-co-stabilized zirconia
CE	counter electrode
DC	direct current
EDX	energy-dispersive X-ray spectroscopy
GDC10	$\text{Ce}_{0.9}\text{Gd}_{0.1}\text{O}_{2-\delta}$
GOF	goodness of fit
RE	reference electrode
SEM	scanning electron microscopy
SG	space group
SOFC	solid oxide fuel cell
SOEC	solid oxide electrolysis cell
TEC	average linear thermal expansion coefficient
TGA	thermogravimetric analysis
WE	working electrode
XRD	X-ray diffraction

### List of symbols

$a$	unit cell parameter
$F$	Faraday constant
$G$	total Gibbs energy
$G^0$	standard Gibbs energy
$\Delta G_i^0$	standard free Gibbs energy of defect formation reaction
$\Delta H_i^0$	enthalpy of defect formation reaction
$\Delta h_{\text{O}}$	enthalpy of oxygen incorporation in the lattice
$i$	current density
$i_0$	exchange current density

$K_d$	equilibrium constant of charge disproportionation reaction
$K_e$	equilibrium constant of electron exchange reaction
$K_{ox}$	equilibrium constant of iron oxidation reaction
$n$	number of electrons participating in the rate-determining step
$p(O_2)$	oxygen partial pressure
$R$	molar gas constant
$r_A$	average radius of A-cation
$r_B$	average radius of B-cations
$R_\eta$	polarization resistance
$r_{O^{2-}}$	radius of oxygen anion
$S_{conf}$	total configurational entropy
$\Delta S_i^0$	entropy of defect formation reaction
$\Delta s_O$	entropy of oxygen incorporation in the lattice
$T$	absolute temperature
$t$	Goldschmidt tolerance factor
$w$	number of anion sites unavailable for oxygen ions
$wR$	weighted profile R-factor
$wR_{min}$	expected R-factor
$\alpha, \beta$	charge transfer coefficients
$\delta$	oxygen nonstoichiometry
$\Delta\delta_{ref}$	parameter for correction of experimental data on the oxygen content
$\varepsilon_{chem}$	isothermal chemical expansion
$\eta$	overpotential
$\theta$	diffraction angle
$\mu_i^0$	standard chemical potential
$\Delta\mu_O$	oxygen chemical potential
$\sigma$	total electrical conductivity

## References

- Das, T.; Nicholas, J.D.; Qi, Y. Long-range charge transfer and oxygen vacancy interactions in strontium ferrite. *J. Mater. Chem. A* **2017**, *5*, 4493–4506. [[CrossRef](#)]
- Sereda, V.; Sednev, A.; Tsvetkov, D.; Zuev, A. Enthalpy increments and redox thermodynamics of SrFeO<sub>3- $\delta$</sub> . *J. Mater. Res.* **2019**, *34*, 3288–3295. [[CrossRef](#)]
- Sereda, V.; Tsvetkov, D.; Ivanov, I.; Zuev, A. Interplay between chemical strain, defects and ordering in Sr<sub>1-x</sub>La<sub>x</sub>FeO<sub>3</sub> materials. *Acta Mater.* **2019**, *162*, 33–45. [[CrossRef](#)]
- Patrakeev, M.; Leonidov, I.; Kozhevnikov, V.; Kharton, V. Ion–electron transport in strontium ferrites: Relationships with structural features and stability. *Solid State Sci.* **2004**, *6*, 907–913. [[CrossRef](#)]
- Merkulov, O.; Naumovich, E.; Patrakeev, M.; Markov, A.; Bouwmeester, H.J.; Leonidov, I.; Kozhevnikov, V. Oxygen nonstoichiometry and defect chemistry of perovskite-structured SrFe<sub>1-x</sub>Mo<sub>x</sub>O<sub>3- $\delta$</sub>  solid solutions. *Solid State Ion.* **2016**, *292*, 116–121. [[CrossRef](#)]
- Savinskaya, O.A.; Nemudry, A.P.; Lyakhov, N.Z. Synthesis and properties of SrFe<sub>1-x</sub>M<sub>x</sub>O<sub>3-z</sub> (M=Mo, W) perovskites. *Inorg. Mater.* **2007**, *43*, 1350–1360. [[CrossRef](#)]
- Zhu, Z.; Wei, Z.; Zhao, Y.; Chen, M.; Wang, S. Properties characterization of tungsten doped strontium ferrites as cathode materials for intermediate temperature solid oxide fuel cells. *Electrochim. Acta* **2017**, *250*, 203–211. [[CrossRef](#)]
- Zhang, M.; Du, Z.; Zhang, Y.; Zhao, H. Progress of Perovskites as Electrodes for Symmetrical Solid Oxide Fuel Cells. *ACS Appl. Energy Mater.* **2022**, *5*, 13081–13095. [[CrossRef](#)]
- Hui, S.; Petric, A. Conductivity and stability of SrVO<sub>3</sub> and mixed perovskites at low oxygen partial pressures. *Solid State Ion.* **2001**, *143*, 275–283. [[CrossRef](#)]
- Macías, J.; Yaremchenko, A.; Frade, J. Redox transitions in strontium vanadates: Electrical conductivity and dimensional changes. *J. Alloys Compd.* **2014**, *601*, 186–194. [[CrossRef](#)]
- Macías, J.; Yaremchenko, A.A.; Fagg, D.P.; Frade, J.R. Structural and defect chemistry guidelines for Sr(V,Nb)O<sub>3</sub>-based SOFC anode materials. *Phys. Chem. Chem. Phys.* **2015**, *17*, 10749–10758. [[CrossRef](#)]

12. Yaremchenko, A.; Brinkmann, B.; Janssen, R.; Frade, J. Electrical conductivity, thermal expansion and stability of Y- and Al-substituted SrVO<sub>3</sub> as prospective SOFC anode material. *Solid State Ion.* **2013**, *247–248*, 86–93. [[CrossRef](#)]
13. Ge, X.; Chan, S.; Liu, Q.; Sun, Q. Solid Oxide Fuel Cell Anode Materials for Direct Hydrocarbon Utilization. *Adv. Energy Mater.* **2012**, *2*, 1156–1181. [[CrossRef](#)]
14. Aguilar, L.; Zha, S.; Cheng, Z.; Winnick, J.; Liu, M. A solid oxide fuel cell operating on hydrogen sulfide (H<sub>2</sub>S) and sulfur-containing fuels. *J. Power Sources* **2004**, *135*, 17–24. [[CrossRef](#)]
15. Cheng, Z.; Zha, S.; Aguilar, L.; Liu, M. Chemical, electrical, and thermal properties of strontium doped lanthanum vanadate. *Solid State Ion.* **2005**, *176*, 1921–1928. [[CrossRef](#)]
16. Jiang, S.; Sunarso, J.; Zhou, W.; Shen, J.; Ran, R.; Shao, Z. Cobalt-free SrNb<sub>x</sub>Fe<sub>1-x</sub>O<sub>3-δ</sub> (x = 0.05, 0.1 and 0.2) perovskite cathodes for intermediate temperature solid oxide fuel cells. *J. Power Sources* **2015**, *298*, 209–216. [[CrossRef](#)]
17. Anikina, P.V.; Markov, A.A.; Patrakeev, M.V.; Leonidov, I.A.; Kozhevnikov, V.L. High-temperature transport and stability of SrFe<sub>1-x</sub>Nb<sub>x</sub>O<sub>3-δ</sub>. *Solid State Sci.* **2009**, *11*, 1156–1162. [[CrossRef](#)]
18. Zhang, Y.; Gao, X.; Sunarso, J.; Liu, B.; Zhou, W.; Ni, M.; Shao, Z. Significantly Improving the Durability of Single-Chamber Solid Oxide Fuel Cells: A Highly Active CO<sub>2</sub>-Resistant Perovskite Cathode. *ACS Appl. Energy Mater.* **2018**, *1*, 1337–1343. [[CrossRef](#)]
19. Qiu, H.; Liang, M.; Zhao, J.; Liang, Z.; Jiang, S.; Shi, H.; Wang, W.; Wen, H.; Su, C. A-site cation deficient SrTa<sub>0.1</sub>Fe<sub>0.9</sub>O<sub>3-δ</sub> as a bi-functional cathode for both oxygen ion- and proton-conducting solid oxide fuel cells. *Ceram. Int.* **2024**, *50*, 40500–40509. [[CrossRef](#)]
20. Xu, S.; Qiu, H.; Jiang, S.; Jiang, J.; Wang, W.; Xu, X.; Kong, W.; Chivurugwi, T.D.; Proskurin, A.; Chen, D.; et al. New strategy for boosting cathodic performance of low temperature solid oxide fuel cells via chlorine doping. *Nano Res.* **2024**, *17*, 8086–8094. [[CrossRef](#)]
21. Nakayama, N.; Takano, M.; Inamura, S.; Nakanishi, N.; Kosuge, K. Electron microscopy study of the “cubic” perovskite phase SrFe<sub>1-x</sub>V<sub>x</sub>O<sub>2.5+x</sub> (0.05 ≤ x ≤ 0.1). *J. Solid State Chem.* **1987**, *71*, 403–417. [[CrossRef](#)]
22. Ancharova, U.V.; Cherepanova, S.V. Nano-domain states of strontium ferrites SrFe<sub>1-y</sub>M<sub>y</sub>O<sub>2.5+x</sub> (M=V, Mo; y ≤ 0.1; x ≤ 0.2). *J. Solid State Chem.* **2015**, *225*, 410–416. [[CrossRef](#)]
23. Ancharova, U.V.; Cherepanova, S.V.; Petrov, S.A. Adaptation ways for a high concentration oxygen vacancies in nonstoichiometric strontium ferrites. *J. Struct. Chem.* **2017**, *58*, 53–61. [[CrossRef](#)]
24. Ramesha, K.; Gopalakrishnan, J.; Smolyaninova, V.; Greene, R. ALaFeVO<sub>6</sub> (A=Ca, Sr): New Double-Perovskite Oxides. *J. Solid State Chem.* **2001**, *162*, 250–253. [[CrossRef](#)]
25. Kharton, V.; Tsipis, E.; Marozau, I.; Viskup, A.; Frade, J.; Irvine, J. Mixed conductivity and electrochemical behavior of (La<sub>0.75</sub>Sr<sub>0.25</sub>)<sub>0.95</sub>Cr<sub>0.5</sub>Mn<sub>0.5</sub>O<sub>3-δ</sub>. *Solid State Ion.* **2007**, *178*, 101–113. [[CrossRef](#)]
26. Nikitin, S.; Dyakina, M.; Tsipis, E.; Patrakeev, M. Oxygen nonstoichiometry, electrical conductivity, and electrochemical activity of La<sub>0.45</sub>Ce<sub>0.05</sub>Sr<sub>0.5</sub>FeO<sub>3-δ</sub>. *J. Power Sources* **2024**, *597*, 234115. [[CrossRef](#)]
27. Hidayat, T.; Shishin, D.; Jak, E.; Decterov, S.A. Thermodynamic reevaluation of the Fe–O system. *Calphad* **2015**, *48*, 131–144. [[CrossRef](#)]
28. Kuhn, M.; Hashimoto, S.; Sato, K.; Yashiro, K.; Mizusaki, J. Oxygen nonstoichiometry, thermo-chemical stability and lattice expansion of La<sub>0.6</sub>Sr<sub>0.4</sub>FeO<sub>3-δ</sub>. *Solid State Ion.* **2011**, *195*, 7–15. [[CrossRef](#)]
29. Oishi, M.; Yashiro, K.; Sato, K.; Mizusaki, J.; Kawada, T. Oxygen nonstoichiometry and defect structure analysis of B-site mixed perovskite-type oxide (La, Sr)(Cr, M)O<sub>3-δ</sub> (M=Ti, Mn and Fe). *J. Solid State Chem.* **2008**, *181*, 3177–3184. [[CrossRef](#)]
30. Mizusaki, J.; Yoshihiro, M.; Yamauchi, S.; Fueki, K. Thermodynamic quantities and defect equilibrium in the perovskite-type oxide solid solution La<sub>1-x</sub>Sr<sub>x</sub>FeO<sub>3-δ</sub>. *J. Solid State Chem.* **1987**, *67*, 1–8. [[CrossRef](#)]
31. Non-Linear Least-Squares Minimization and Curve-Fitting for Python. Available online: <https://lmfit.github.io/lmfit-py/> (accessed on 1 November 2023).
32. Yoo, J.; Yoo, C.; Yu, J.; Jacobson, A.J. Determination of oxygen nonstoichiometry in SrFeO<sub>3-δ</sub> by solid-state Coulometric titration. *J. Am. Ceram. Soc.* **2017**, *100*, 2690–2699. [[CrossRef](#)]
33. Dezsó, A.; Kaptay, G. On the Configurational Entropy of Nanoscale Solutions for More Accurate Surface and Bulk Nano-Thermodynamic Calculations. *Entropy* **2017**, *19*, 248. [[CrossRef](#)]
34. Istomin, S.Y.; Lyskov, N.V.; Mazo, G.N.; Antipov, E.V. Electrode materials based on complex d-metal oxides for symmetrical solid oxide fuel cells. *Russ. Chem. Rev.* **2021**, *90*, 644–676. [[CrossRef](#)]
35. Shannon, R.D. Revised effective ionic radii and systematic studies of interatomic distances in halides and chalcogenides. *Acta Cryst.* **1976**, *A32*, 751–766. [[CrossRef](#)]
36. Lein, H.L.; Wiik, K.; Grande, T. Thermal and chemical expansion of mixed conducting La<sub>0.5</sub>Sr<sub>0.5</sub>Fe<sub>1-x</sub>Co<sub>x</sub>O<sub>3-δ</sub> materials. *Solid State Ion.* **2006**, *177*, 1795–1798. [[CrossRef](#)]
37. Kolotygin, V.A.; Tsipis, E.V.; Markov, A.A.; Patrakeev, M.V.; Waerenborgh, J.C.; Shaula, A.L.; Kharton, V.V. Transport and Electrochemical Properties of SrFe(Al,Mo)O<sub>3-δ</sub>. *Russ. J. Electrochem.* **2018**, *54*, 514–526. [[CrossRef](#)]

38. Hombo, J.; Matsumoto, Y.; Kawano, T. Electrical conductivities of  $\text{SrFeO}_{3-\delta}$  and  $\text{BaFeO}_{3-\delta}$  perovskites. *J. Solid State Chem.* **1990**, *84*, 138–143. [[CrossRef](#)]
39. Svensson, A.M.; Sunde, S.; Nişancıoğlu, K. Mathematical modeling of oxygen exchange and transport in air-perovskite-YSZ interface regions: I. Reduction of intermediately adsorbed oxygen. *J. Electrochem. Soc.* **1997**, *144*, 2719–2732. [[CrossRef](#)]
40. Jiang, S.P. Development of lanthanum strontium cobalt ferrite perovskite electrodes of solid oxide fuel cells—A review. *Int. J. Hydrogen Energy* **2019**, *44*, 7448–7493. [[CrossRef](#)]
41. Ascolani-Yael, J.; Montenegro-Hernández, A.; Garcés, D.; Liu, Q.; Wang, H.; Yakal-Kremski, K.; Barnett, S.; Mogni, L. The oxygen reduction reaction in solid oxide fuel cells: From kinetic parameters measurements to electrode design. *J. Phys. Energy* **2020**, *2*, 042004. [[CrossRef](#)]
42. Anikina, P.V.; Markov, A.A.; Patrakeev, M.V.; Leonidov, I.A.; Kozhevnikov, V.L. The structure, nonstoichiometry, and thermodynamic characteristics of oxygen in strontium ferrite doped with niobium,  $\text{SrFe}_{1-x}\text{Nb}_x\text{O}_{3-\delta}$ , *Russ. J. Phys. Chem. A* **2009**, *83*, 699–704. [[CrossRef](#)]

**Disclaimer/Publisher’s Note:** The statements, opinions and data contained in all publications are solely those of the individual author(s) and contributor(s) and not of MDPI and/or the editor(s). MDPI and/or the editor(s) disclaim responsibility for any injury to people or property resulting from any ideas, methods, instructions or products referred to in the content.